International Journal of Nanomedicine

Dovepress
Taylor & Francis Group

Open Access Full Text Article

ORIGINAL RESEARCH

Metal-Organic Framework Nanoplatform Synergizes Fenton-Driven Ferroptosis and Photodynamic Apoptosis for Enhanced Hepatocellular Carcinoma Therapy

Shasha Kong[1,2,*], Hongmei Lin[3,4,*], Yuling Liu[1,*], Ruying Tang[1], Hui Li[1,2], Longfei Lin[1]

[1]Institute of Chinese Materia Medica, China Academy of Chinese Medical Sciences, Beijing, People's Republic of China; [2]Institute of Traditional Chinese Medicine Health Industry, China Academy of Chinese Medical Sciences, Nanchang, Jiangxi, People's Republic of China; [3]Beijing Research Institute of Chinese Medicine, Beijing University of Chinese Medicine, Beijing, People's Republic of China; [4]National Medical Products Administration Key Laboratory for Research Evaluation of Traditional Chinese Medicine, Beijing University of Chinese Medicine, Beijing, People's Republic of China

*These authors contributed equally to this work

Correspondence: Hui Li; Longfei Lin, Email lihuizys@126.com; lflin@icmm.ac.cn

Background: Hepatocellular carcinoma (HCC) is notorious for its dismal prognosis and resistance to conventional therapies. The integration of multiple cell death mechanisms emerges as a promising strategy to combat the heterogeneity of this malignancy.

Purpose: Herein, we engineered a multifunctional nanoplatform, TPMIL101-TCPP@Lip-HA, by encapsulating the photosensitizer TCPP and chemotherapeutic agent triptolide (TP) within a metal-organic framework (MIL101), followed by surface modification with liposomes and hyaluronic acid. This sophisticated drug delivery system capitalizes on the enhanced permeability and retention effect to achieve tumor-specific accumulation.

Methods: Upon reaching the tumor site, TPMIL101-TCPP@Lip-HA undergoes gradual disintegration, releasing its therapeutic payload. The tumor microenvironment facilitates the reduction of Fe^{3+} to Fe^{2+}, triggering ferroptosis through the Fenton reaction. Simultaneously, laser irradiation activates TCPP to generate cytotoxic reactive oxygen species, initiating photodynamic therapy-induced apoptosis. The concomitant accumulation of lipid peroxides synergistically amplifies the ferroptotic cascade.

Results: *In vitro/in vivo* studies confirm potent anti-HCC efficacy with reduced TP toxicity. Mechanistic studies elucidate that TPMIL101-TCPP@Lip-HA orchestrates ferroptosis through modulation of iron storage and lipid oxidation proteins, while concurrently inducing apoptosis via the cytochrome c/Apaf-1/caspase signaling axis.

Conclusion: These findings collectively underscore TPMIL101-TCPP@Lip-HA as a potent therapeutic nanoplatform capable of arresting HCC progression.

Keywords: hepatocellular carcinoma, Fenton reaction, photodynamic therapy, ferroptosis, apoptosis

Introduction

Hepatocellular carcinoma (HCC), the sixth most prevalent malignancy and third leading cause of cancer-related deaths globally, remains a therapeutic challenge due to late-stage diagnosis and limited treatment efficacy.[1] Despite advancements in HCC management, current therapies are often constrained by severe side effects and drug resistance, highlighting the urgent need for innovative treatment strategies. Triptolide (TP), a potent diterpene triepoxide derived from *Tripterygium wilfordii*, has demonstrated significant anti-tumor activity against HCC at low concentrations.[2–4] However, its clinical application is hindered by poor water solubility, systemic toxicity, and a narrow therapeutic window.[3,5] These limitations underscore the critical need for developing advanced drug delivery systems to enhance TP's therapeutic potential while minimizing its adverse effects, offering a promising avenue for improved HCC therapy.

https://doi.org/10.2147/IJN.S567165
Received: 12 September 2025
Accepted: 23 January 2026
Published: 19 May 2026

Graphical Abstract

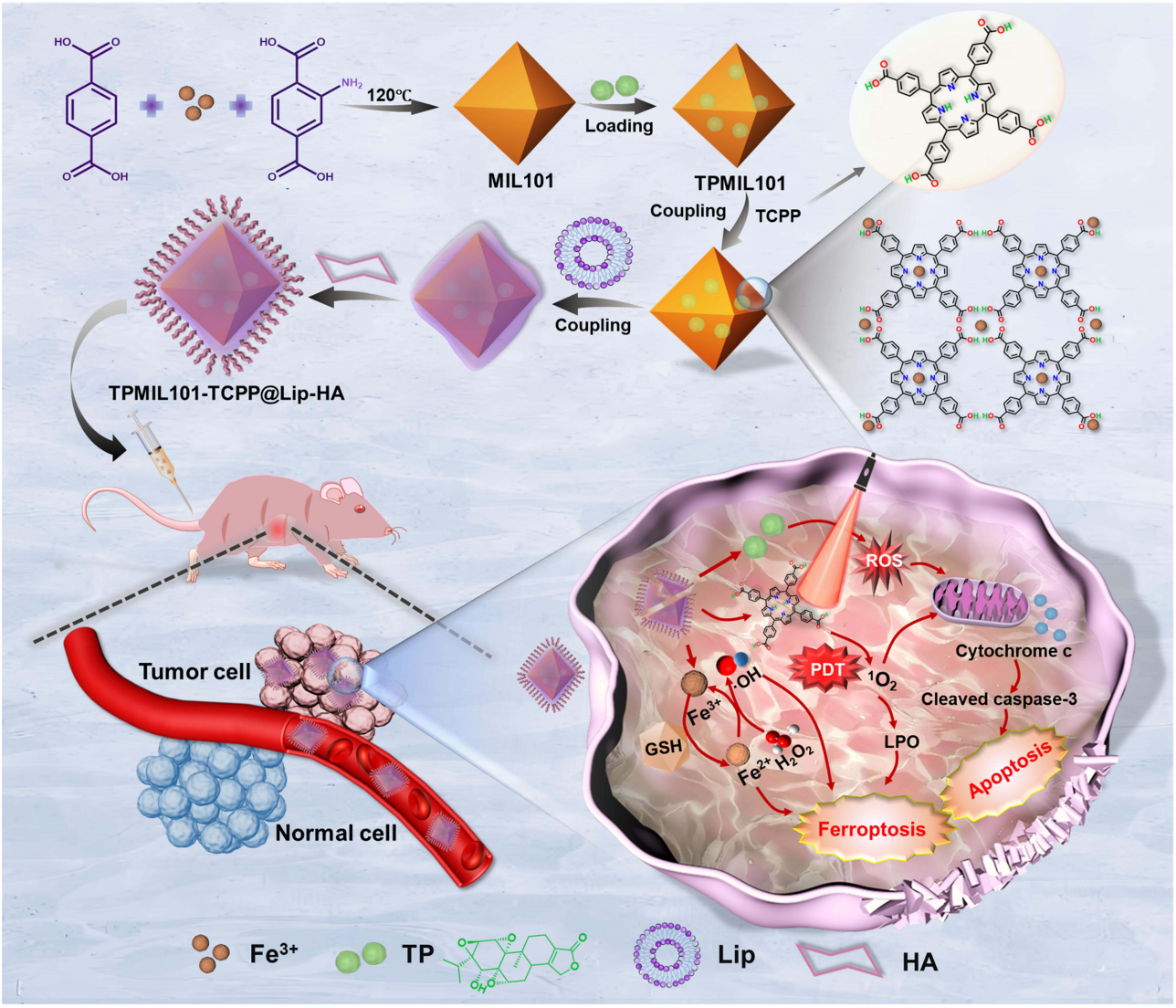

The tumor microenvironment (TME) is characterized by hypoxia, mild acidity, and elevated levels of hydrogen peroxide (H_2O_2) and glutathione (GSH), creating conditions conducive to tumor growth.[6,7] While this complex TME impedes therapeutic efficacy, it also provides opportunities for developing targeted treatment strategies. Over the past decade, numerous TME-responsive nanocomposites have been engineered for cancer treatment, with ferroptosis induced by metal-based nanomaterials emerging as a promising approach. Ferroptosis, as its name suggests, is heavily dependent on intracellular iron ion (redox-active Fe^{2+}) accumulation. Fe^{2+} interacts with peroxides through the Fenton reaction, generating Fe^{3+} and peroxy radicals, predominantly hydroxyl radicals (•OH), which subsequently react with lipids to form lipid peroxides (LPO).[8,9] In the TME, where H_2O_2 and GSH are abundant, a sudden increase in Fe^{3+} in vivo catalyzes its conversion to Fe^{2+}, intensifying the Fenton reaction. This process produces substantial amounts of hydroxyl radicals (•OH) and leads to excessive LPO accumulation, ultimately triggering cell ferroptosis. Consequently, enhancing iron ion transport efficiency to elevate unstable iron levels is crucial for treating ferroptosis-related tumors. Various iron-based nanomaterials have been extensively utilized in designing iron ion delivery systems,[10–13] effectively inducing programmed tumor cell death through additional delivery of Fenton reaction catalysts in vitro. However, tumor heterogeneity implies that a single mode of cell death

may be insufficient to address the diverse subgroups of cancer cells with distinct genotypes and phenotypes. The combination of multiple cell death pathways may offer a potential solution to overcome treatment failures associated with cancer heterogeneity.

Multiple cell death pathways can be effectively combined in cancer therapies based on reactive oxygen species (ROS), such as photodynamic therapy (PDT), sonodynamic therapy (SDT), and chemodynamic therapy (CDT).[14–17] As a selective killing treatment, PDT has gained clinical approval for tumor therapy due to its distinctive advantages, including broad applicability, minimal invasiveness, and low toxicity.[18] The efficacy of PDT relies on the activation of photosensitizers, which generate high levels of ROS that exceed tumor cells tolerance. These ROS interact with intracellular biomacromolecules, leading to mitochondrial damage, promoting Cytochrome c release from mitochondria to the cytoplasm, stimulating over-expression of apoptosis markers such as Caspase-3 and Caspase-9, and consequently activating the mitochondria-mediated apoptosis pathway. Currently, commonly used photosensitizers are primarily porphyrin-based nanocomposites. Mesotetra (4-carboxyphenyl)porphin (TCPP), a member of the porphyrin family, offers unique advantages compared to other photosensitizers (such as rhodamine, coumarin, and anthocyanin). Its strong absorption in the infrared region makes TCPP photosensitizers particularly useful in treating deep-seated tumors.[19] The excellent biological characteristics of TCPP, including good biocompatibility, prolonged tumor residence time, minimal side effects, and effective clearance, contribute to its widespread application in PDT.[20–22] Furthermore, TCPP can coordinate with metal ions to form a metal-organic skeleton (MOF-TCPP) structure without modification.[23] While most photosensitizers are hydrophobic and prone to aggregation quenching.[19] TCPP-based MOFs not only enhance the water solubility of TCPP but also maintain its photosensitive activity even at high doses.[23] MOF-TCPP can also serve as a nano-carrier for TP drug delivery, demonstrating significant potential in biomedical applications. Considering that MOF-TCPP nanoparticles are easily recognized by the body's immune system, potentially triggering immune rejection and rapid clearance, which could impede their anti-tumor pharmacological activity. To overcome this challenge, we enhanced the diversity of terminal chemical groups while preserving the excellent physicochemical properties of MOF-TCPP nanoparticles. TPMIL101-TCPP was encapsulated in liposomes, and the liposome surface was then coated with hyaluronic acid. This approach is expected to improve the biocompatibility of nanoparticles and extend the circulation time of drugs in the body.

In this study, we engineered a liposome-coated, photoactivatable MOF nanoplatform, TPMIL101-TCPP@Lip-HA, co-loaded with TP and the photosensitizer TCPP for HCC therapy. The iron-based MOF component exploits the TME to drive fenton reactions, generating •OH and LPO that disrupt lipid metabolism and induce ferroptosis. Near-infrared laser irradiation activates TCPP, enhancing ROS production for oxygen-dependent PDT and initiating apoptosis via the cytochrome c/Apaf-1/caspase signaling cascade. This innovative platform synergistically integrates ferroptosis and apoptosis mechanisms, demonstrating potent anti-HCC efficacy. Importantly, TPMIL101-TCPP@Lip-HA exhibits excellent biosafety in vivo and significantly reduces TP-associated toxicity. These results highlight the platform's potential as a promising therapeutic strategy for HCC, offering a dual-modal approach to enhance treatment outcomes.

Experimental Section

Cell Lines and Materials

The HCC cell lines HepG2 were acquired from the Shanghai Cell Bank of Type Culture Collection of the Chinese Academy of Sciences. Triptolide (HPLC > 98%) was procured from Baoji Yirui Biotechnology Co., LTD (Shaanxi, China). Terephthalic acid (H_2BDC), 2-amino terephthalic acid ($H_2BDC\text{-}NH_2$), cholesterol, phospholipid polyethylene glycol derivatives ($DSPE\text{-}PEG_{2000}$), and Soy phosphatidylcholine (SPC) were obtained from Xi'an Ruixi Biotechnology Co., LTD (Xian, China). $FeCl_3 \cdot 6H_2O$ was supplied by Beijing Yinokai Technology Co., LTD (Beijing, China). 1, 3-diphenyl isobenzofuran (DPBF) was sourced from MedChemExpress LLC (NJ, USA). 3,3′,5,5′-tetramethylbenzidine (TMB) and indocyanine green (ICG) were procured from Shanghai Yuanye Biotechnology Co., LTD (Shanghai, China). Primary antibodies against FTL (10727-1-AP), FTH (83428-1-RR), FSP1 (20886-1-AP), GPX4 (67763-1-Ig), COX2 (27308-1-AP), BAX (50599-2-Ig), BCL2 (12789-1-AP), Cytochrome c (10993-1-AP), and Cleaved Caspase 3 (82707-13-RR) were purchased from Proteintech Group Incorporated (Wuhan, China) Anti-GAPDH was also obtained from Proteintech Group Incorporated (Wuhan, China).

Synthesis of TPMIL101-TCPP@Lip-HA

Synthesis of TPMIL101: TPMIL101 was synthesized in a two-step process. First, MIL101 was prepared using the solvothermal method, following established protocols.[24] 0.0622g H_2BDC, 0.0667g $H_2BDC\text{-}NH_2$, and 0.0699g $FeCl_3 \cdot 6H_2O$ were dissolved in 100 mL DMF. The resulting solution was sealed in a Teflon-lined stainless steel autoclave and heated at 120 °C for 12 h. After cooling to room temperature, the mixture was centrifuged at 12,000 rpm for 5 min. The precipitate was washed thrice with ethanol and dispersed in water to obtain the MIL101 solution. Subsequently, 0.1502 g of TP was dissolved in 15 mL of DMF and thoroughly combined with the pre-formed MIL101 aqueous solution, stirring at room temperature for 12 h. Following centrifugation at 12000 rpm for 5 min, the resulting precipitates were washed successively with ethanol and water to yield TPMIL101.

Synthesis of TPMIL101@Lip: 2.8 g SPC, 0.8 g cholesterol, and 0.4 g DSPE-PEG_{2000} were weighed and fully dissolved in 4 mL chloroform. The solution was transferred to a round-bottomed flask and evaporated at 60 °C under reduced pressure using a rotary evaporator. Blank liposomes were hydrated with 2.5 mL of deionized water. Subsequently, 2.5 mL of 40% TPMIL101 aqueous solution was added, and the mixture underwent ultrasonic treatment at 20 °C for 5 min at 100 W. The resulting mixture was extruded at room temperature using a liposome extruder (Polycarbonate membrane, pore size 200 nm; Avanti, USA). Finally, the volume was adjusted to 5 mL with deionized water. A freeze-drying protectant was added prior to lyophilization.

Synthesis of TPMIL101-TCPP@Lip: 2.8 g SPC, 0.8 g cholesterol, and 0.4 g DSPE-PEG_{2000} were fully dissolved in 4 mL chloroform. TCPP was dissolved in methanol. Both solutions were transferred to a round-bottomed flask and evaporated at 60 °C under reduced pressure using a rotary evaporator. The blank liposomes were hydrated with 2.5 mL of deionized water. Subsequently, 2.5 mL of 40% TPMIL101 aqueous solution was added, followed by ultrasonic treatment at 20 °C for 5 min. The mixture was then extruded at room temperature using a liposome extruder (Polycarbonate membrane, pore size 200 nm; Avanti, USA). Finally, deionized water was added to achieve a total volume of 5 mL. A freeze-drying protectant was added before lyophilization.

Synthesis of TPMIL101-TCPP@Lip-HA: 2.8 g SPC, 0.8 g cholesterol, and 0.4 g DSPE-PEG_{2000} were fully dissolved in 4 mL chloroform. TCPP was dissolved in methanol. Both solutions were transferred to a round-bottomed flask and evaporated at 60 °C under reduced pressure using a rotary evaporator. For hydration, 2.5 mL of 7% DSPE-PEG_{2000}-HA aqueous solution was utilized. Subsequently, 2.5 mL of 40% TPMIL101 aqueous solution was added, followed by ultrasonic treatment. The mixture was extruded at room temperature using a liposome extruder (Polycarbonate membrane, pore size 200 nm; Avanti, USA). The final volume was adjusted to 5 mL with deionized water. A freeze-drying protectant was added prior to lyophilization.

Synthesis of ICG/TPMIL101-TCPP@Lip-HA: To visualize the distribution of nanomaterials in vivo, ICG/TPMIL101-TCPP@Lip-HA was prepared. First, ML101 was re-dispersed in DMF, and ICG was dissolved in DMF before being added to the MIL101 solution. This mixture was stirred at room temperature for 12 h. Following centrifugation at 12000 rpm for 5 min, the resulting precipitates were washed successively with ethanol and water to obtain ICGMIL101. In a separate process, SPC and cholesterol were dissolved in chloroform, while TCPP was dissolved in methanol. These solutions were transferred to a round-bottom flask, mixed evenly, then evaporated to form a thin film under reduced pressure. Afterward, an aqueous solution of DSPE-PEG_{2000}-HA was added for hydration. Subsequently, the ICGMIL101 aqueous dispersion was incorporated into the mixture. This combined solution underwent ultrasonic treatment and was processed using a liposome extruder. Finally, deionized water was added to achieve a final volume of 5 mL. A freeze-drying protectant was added before lyophilization.

Characterization

The hydrodynamic size, polydispersity index (PDI), and zeta potentials were measured using a NanoBrook 90plus PALS nanosize potentiometer (Brookhaven, USA). Transmission electron microscopy (TEM) images were obtained using a TF20 microscope (FEI Company, USA). X-ray diffraction (XRD) analysis was performed on a D8 Advance system (BrukerAXS, Germany). X-ray photoelectron spectroscopy (XPS) was conducted using a K-Alpha™ XPS instrument (Thermo Scientific, USA) to analyze the elemental composition and distribution of MIL101. The 200–400 nm spectrum was recorded using an ultraviolet-visible spectrometer (Beijing Purkinje General Instrument Co., LTD., China).

Drug Loading and Release

During the preparation of TPMIL101-TCPP@Lip-HA, all supernatants were collected, and the absorbance values of TP (220 nm) and TCPP (414 nm) were measured using a UV-Vis spectrophotometer. The weight of unloaded drugs was calculated according to the standard curves of TP and TCPP. The drug loading capacity (DLC) and drug encapsulation efficiency (DEE) were determined using formulas 1 and 2.

$$\mathrm{DLC}\,(\%) = \frac{\text{weight of loaded drug}}{\text{weight of whole nanoparticles}} \times 100 \tag{1}$$

$$\mathrm{DEE}\,(\%) = \frac{\text{weight of loaded drug}}{\text{weight of fed drug initially}} \times 100 \tag{2}$$

2 mL solutions of TPMIL101 and TPMIL101-TCPP@Lip-HA (10 mg/mL) were placed in dialysis bags (MW 3500 Da) and incubated with 49 mL PBS buffer (pH 7.4 or pH 5.5) at 37 °C to assess cumulative drug release capacity. Samples of the external PBS were collected at 0, 2, 4, 6, 8, 24, and 48 h, with an equal volume of fresh PBS solution replenished after each sampling. The absorbance values of TP and TCPP in the PBS samples were measured using a UV-Vis spectrophotometer to quantify the drug release.

Evaluation of Photocatalytic Performance

TMB solution was obtained by 10.21 mg TMB dispersed in 1 mL DMSO. Subsequently, 20 μL of TMB, 25 μg/mL of TPMIL101-TCPP@Lip-HA, and 5 μL of H_2O_2 were dispersed in water. This mixed solution was treated with or without laser irradiation for 5 min, and the UV-Vis spectra of the supernatant in the range of 550–750 nm were recorded. Additionally, under the same conditions, peroxidase was used as a positive control, and the mixed solution underwent laser-free treatment before recording the UV-Vis spectra. Deionized water was used as a blank control, and the mixed solution was treated with or without laser irradiation, followed by recording the UV-Vis spectrum.

Photoinduced Hydroxyl Radical Detection

The H_2BDC fluorescent probe was utilized to assess the hydroxyl radical (•OH) production capacity of TPMIL101-TCPP @Lip-HA. 0.0069g of H_2BDC was dispersed in 10 mL of deionized water, with NaOH added dropwise. The solution was heated and stirred to facilitate dissolution. For the experiment, 20 μg of TPMIL101-TCPP@Lip-HA was dispersed in 1 mL of PBS buffer solution, to which 80 μL of H_2BDC solution was added. Deionized water served as the control group. The samples were subjected to both laser and no-laser conditions. Following treatment, particles were removed via centrifugation, and fluorescence analysis was performed on the supernatant. The excitation filter was set to 315 nm, with the emission filter ranging from 350–600 nm. To investigate the laser excitation time of TPMIL101-TCPP@Lip-HA, fluorescence intensity was measured at intervals of 0, 2, 4, 6, 8, and 10 min of laser exposure.

Photoinduced Singlet Oxygen Detection

The generation of singlet oxygen ($^1O_2^-$) by TPMIL101-TCPP@Lip-HA in vitro was evaluated using 1,3-diphenylisofenofuran (DPBF) and singlet oxygen sensor green (SOSG) probes. A 1 mg/mL DPBF solution was prepared using DMF as the solvent, while the TPMIL101-TCPP@Lip-HA sample was dispersed in a 50% DMF solution. For each 1 mL sample solution, 80 μL of DPBF reagent was added, followed by treatment with or without laser irradiation. The suspension was then centrifuged to remove particles, and the supernatant's absorbance was measured at 410 nm using a UV-Vis spectrophotometer. For $^1O_2^-$ detection using the SOSG probe, 1 μL of 2.5 μM SOSG methanol solution was added to each 1 mL sample solution, followed by laser or no laser treatment. After centrifugation, the supernatant's fluorescence was measured with an excitation filter set at 488 nm and an emission filter range of 500–600 nm.

Antitumor Activity in vitro

Cell Culture and in vitro Cytotoxicity

HepG2 cells (8×10^3) were seeded in 96-well plates and incubated overnight. The cells were then exposed to 100 μL of drug-containing medium at varying concentrations (TP, TPMIL101, TPMIL101@Lip, TPMIL101-TCPP@Lip, and TPMIL101-TCPP@Lip-HA; 2.5–80 μg/mL) for 24 h. Subsequently, the drug-containing medium was replaced with 100 μL of 10% CCK8 solution and incubated at 37 °C for 1 h. The optical density (OD) values of each well were measured at 450 nm using a microplate reader.

To assess phototoxicity, cells in each experimental group were incubated with 100 μL of drug-containing medium (TP, 10 μg/mL) for 16 h. Subsequently, the cells were exposed to an 808 nm laser at 1.0 W/cm^2 for 8 min, followed by an additional 8-hour incubation period. The viability of cells in each group was then evaluated using a CCK-8 assay.

Calcein-AM/PI Double Staining

HepG2 cells were seeded at a density of 1×10^5 cells/well in a 35 mm glass bottom confocal culture dish and incubated overnight. The culture medium was then replaced with 1 mL of drug-containing medium (equivalent to 10 μg/mL TP concentration), and cells in the TP, TPMIL101, and TPMIL101@Lip groups were treated for 24 h. For the TPMIL101-TCPP@Lip + L and TPMIL101-TCPP@Lip-HA + L groups, 16 h post-administration, 808 nm laser irradiation (1.0 W/cm^2) was applied for 8 min, followed by an additional 8 h incubation. Subsequently, cells were stained with Calcein-AM/PI working solution (Beyotime Biotechnology Co., LTD, Shanghai, China) at 37 °C for 30 min in darkness. Four random images per group were captured using a Leica confocal microscope (DMI 600B, Wetzlar, Germany). Green fluorescence was detected using excitation/emission filters at 494/517 nm, while red fluorescence was detected at 535/617 nm.

Determination of Intracellular Fe^{2+} Concentration

HepG2 cells (6×10^5 cells/well) were seeded in 6-well plates and incubated overnight. The medium was subsequently replaced with a drug-containing medium (equivalent concentration of 10 μg/mL TP). Cells in TP, TPMIL101, and TPMIL101@Lip groups underwent continuous treatment for 24 h. For TPMIL101-TCPP@Lip + L and TPMIL101-TCPP@Lip-HA + L groups, 16 h post-administration, 808 nm (1.0 W/cm^2) laser irradiation was applied for 8 min, followed by an additional 8 h incubation. Intracellular Fe^{2+} levels were measured according to the instructions provided by the Fe^{2+} kit (Solaibao Biotechnology Co., LTD., China).

Intracellular ROS Generation Measured

HepG2 cells (1×10^5 cells/well) were seeded in a 35 mm glass bottom confocal culture dish and incubated overnight. The medium was then replaced with a drug-containing medium (equivalent concentration of 10 μg/mL TP). Cells in TP, TPMIL101, and TPMIL101@Lip groups were treated continuously for 24 h. For TPMIL101-TCPP@Lip + L and TPMIL101-TCPP@Lip-HA + L groups, after 16 h of treatment with drug-containing medium, an 808 nm (1.0 W/cm^2) laser was applied for 8 min, followed by an additional 8 h incubation. Under dark conditions, the cells were incubated with 10 mM DCFH (Beyotime Biotechnology Co., LTD., China) for 20 min. A confocal microscope captured 4 random images in each group with excitation and emission filters set to 488/525 nm.

Intracellular Malondialdehyde (MDA), GSH Assay

HepG2 cells (6×10^5 cells/well) were seeded in 6-well plates and incubated overnight. Cells in the TP, TPMIL101, and TPMIL101@Lip groups were treated with a fresh drug-containing medium (equivalent concentration of 10 μg/mL TP) for 24 h. After 16 h of treatment with fresh drug-containing medium, cells in the TPMIL101-TCPP@Lip + L and TPMIL101-TCPP@Lip-HA + L groups were irradiated with an 808 nm (1.0 W/cm^2) laser for 8 min, and then incubated for an additional 8 h. Intracellular MDA and GSH levels were measured according to the instructions provided with the MDA and GSH kits (Beyotime Biotechnology Co., LTD., China).

Intracellular Lipid Peroxide (LPO) Assay

HepG2 cells (1×10^5 cells/well) were seeded in a 35 mm glass bottom confocal culture dish and incubated overnight. Cells in TP, TPMIL101, and TPMIL101@Lip groups were exposed to fresh drug-containing medium (equivalent

concentration of 10 μg/mL TP) for 24 h. The TPMIL101-TCPP@Lip + L and TPMIL101-TCPP@Lip-HA + L groups were treated with drug-containing medium for 16 h, irradiated with an 808 nm (1.0 W/cm^2) laser for 8 min, and then incubated for an additional 8 h. A 10 μM Liperfluo working solution (Dojindo Laboratories, Japan) was applied and incubated at 37 °C for 30 min. Cell images were captured randomly using confocal microscopy with an excitation filter of 488 nm and an emission filter of 525 nm.

Nuclear Morphology

HepG2 cells (1 × 10^5 cells/well) were seeded in a 35 mm glass bottom confocal culture dish and incubated overnight. Cells in TP, TPMIL101, and TPMIL101@Lip groups were treated with fresh drug-containing medium (equivalent concentration of 10 μg/mL TP) for 24 h. The TPMIL101-TCPP@Lip + L and TPMIL101-TCPP@Lip-HA + L groups were exposed to drug-containing medium for 16 h, irradiated with an 808 nm (1.0 W/cm^2) laser for 8 min, and then incubated for an additional 8 h. Subsequently, cells were fixed with 4% paraformaldehyde at room temperature for 15 min, washed with PBS three times, and incubated with DAPI solution in darkness for 5 min. Nuclear images were captured randomly using a confocal microscope with an excitation filter of 360 nm and an emission filter of 460 nm.

Apoptosis Assay

HepG2 cells (6 × 10^5 cells/mL) were seeded on 6-well plates and incubated overnight. Cells in the TP, TPMIL101, and TPMIL101@Lip groups were continuously exposed to fresh drug-containing medium (equivalent concentration of 10 μg/mL TP) for 24 h. The TPMIL101-TCPP@Lip + L and TPMIL101-TCPP@Lip-HA + L groups were treated with drug-containing medium for 16 h, irradiated with an 808 nm (1.0 W/cm^2) laser for 8 min, and then incubated for an additional 8 h. Annexin V-FITC and PI staining were conducted following the kit instructions (Beyotime Biotechnology Co., LTD., China). The samples were filtered through a nylon mesh (300 mesh) and analyzed using flow cytometry (FCM, BD LTD., USA).

Mitochondrial Membrane Potential (Δψ) Detection

HepG2 cells were seeded on 6-well plates (6 × 10^5 cells /mL) and cultured overnight. The cells were then exposed to fresh drug-containing medium, with the laser group receiving laser treatment. Subsequently, cells were harvested and incubated with JC-1 working solution at 37 °C for 20 min, following the kit instructions provided by Beyotime Biotechnology Co., LTD. Flow cytometry was utilized to measure the mitochondrial membrane potential (Δψ).

Morphological Observation of Mitochondria

HepG2 cells were seeded in 6-well plates (6 × 10^5 cells/mL) and incubated overnight. The cells were then exposed to fresh medium containing the drug (10 μg/mL TP) for 24 h. For the laser-treated groups (TPMIL101-TCPP@Lip + L and TPMIL101-TCPP@Lip-HA + L), after 16 h of incubation, an 808 nm laser (1.0 W/cm^2) was applied for 8 min, followed by an additional 8 h of incubation. Subsequently, the cells were fixed with 2.5% glutaraldehyde, dehydrated, embedded, sectioned, and stained with uranyl acetate and lead citrate. Morphological changes in mitochondria were examined using TEM (Hitachi HT7800, Japan).

Antitumor Activity in vivo

Male BALB/c nude mice (12–14 g) were obtained from SPF (Beijing) Biotechnology Co., LTD. All animal experiments were conducted in accordance with the Regulations on the Administration of Experimental Animals. The experimental protocols were approved by the Animal Ethics Committee of the Institute of Chinese Materia Medica, China Academy of Chinese Medical Sciences (2024B351). The authors adhered to the ARRIVE guidelines.

To establish the hepatocellular carcinoma-derived xenograft (HCC-CDX) model, 100 μL of HepG2 cells (4 × 10^7) suspended in PBS/Matrigel (v/v, 1:1) were injected subcutaneously into the right axillary region of mice. Tumor volume was monitored and calculated using the formula: Tumor volume = 0.5 × (tumor width)^2 × (tumor length). When the tumor volume reached 150 mm^3, mice were randomly assigned to control, TP (1%DMSO solubilization), TPMIL101, TPMIL101@Lip, TPMIL101-TCPP@Lip, TPMIL101-TCPP@Lip + L, TPMIL101-TCPP@Lip-HA, and TPMIL101-TCPP@Lip-HA + L groups (n = 6). On days 1, 3, 5, 7, 9, and 11, each group received drug injections (including TP

0.4mg/kg) via the tail vein. On days 2, 4, and 6, mice in the TPMIL101-TCPP@Lip + L and TPMIL101-TCPP@Lip-HA + L groups were irradiated with an 808 nm laser (1 W/cm,^{2} 10 min). Body weight and tumor volume (V, mm^3) were measured every two days. On day 13, the mice were anesthetized via inhalation of 5% isoflurane (2 L/min flow rate), and blood samples were collected via eyeball extraction, with a volume of 0.7 mL, and this was done only once. After blood collection, the animals were euthanasia by cervical dislocation. Tumors and organs (liver, heart, spleen, lung, and kidney) were harvested, and the tumors were weighed and photographed. Tumor suppression rate (TSR) was calculated using the formula: TSR = (tumor mass in the control group – tumor mass in the treatment group) / tumor mass in the control group × 100%. Tumors (from the first three mice in each group) and organs were preserved in 4% (w/v) paraformaldehyde. Hematoxylin and eosin (H&E) staining, terminal deoxynucleotidyl transferase dUTP nick-end labeling (TUNEL) analysis, and immunohistochemical staining of Ki67 were performed. Additionally, fresh mouse tumors (for each group, the last three mice) were preserved at −80 °C for subsequent Western blotting.

Tissue Distribution

For in vivo fluorescence imaging, TPMIL101-TCPP@Lip-HA nanoparticles were labeled with fluorescent dye ICG, and the HCC-CDX model was established. When the tumor volume reached 200 mm^3, mice were administered free ICG and ICG/TPMIL101-TCPP@Lip-HA (0.1 mL, containing 200 μg ICG) via tail vein injection. Fluorescence imaging was conducted using the IVIS Lumina III imaging system (Caliper, USA) at 24, 48, 72, and 120 h post-administration, with an excitation wavelength of 787 nm and emission wavelength of 815 nm. At 120 h post-administration, the mice were euthanized, tumors and tissues were harvested, and fluorescence imaging was conducted ex vivo.

Western Blotting

Total protein was extracted from tumor tissues. Protein concentration of each sample was determined using a BCA protein assay kit (Beyotime Biotechnology Co., LTD., China). Protein samples (30 μg) were separated by SDS-PAGE gel electrophoresis and transferred to PVDF membranes. The membranes were blocked with 5% skim milk at room temperature for 2 h, followed by incubation with primary antibodies at 4 °C overnight and secondary antibodies at room temperature for 2 h. Finally, the ECL Western blotting detection system was utilized to detect signals from each group.

Detection of Blood Biochemical Indexes

Mouse whole blood samples were centrifuged at 4 °C and 7000 rpm for 5 min to isolate serum. The serum levels of glutamic-pyruvic aminotransferase (GPT), glutamic-oxalic aminotransferase (GOT), and urea nitrogen (BUN) were measured following the manufacturer's kit instructions (Solaibao Technology Co., LTD., Beijing, China). The serum levels of creatinine (Cr) were measured following the manufacturer's kit instructions (Elabscience Biotechnology Co., LTD., Wuhan, China).

Statistical Analysis

Experimental data are presented as mean ± standard deviation (SD). Statistical analysis was performed using GraphPad Prism 6.02 software. Differences between groups were evaluated using an unpaired Student's *t*-test, while comparisons among multiple groups were conducted using a one-way analysis of variance (ANOVA). Statistical significance was determined at *P < 0.05, **P < 0.01, and ***P < 0.001 levels.

Results

Synthesis and Characterization of TPMIL101-TCPP@Lip-HA

The synthesis pathway of TPMIL101-TCPP@Lip-HA is illustrated in Graphical Abstract. To confirm the success of the modification process, each step was evaluated. The XRD pattern of MIL101 material exhibited a characteristic diffraction peak of the crystal at approximately 10° (Figure S1), while TEM images revealed that MIL101 displayed regular octahedral structural characteristics (Figure 1A), indicating successful MIL101 synthesis. TPMIL101 demonstrated three

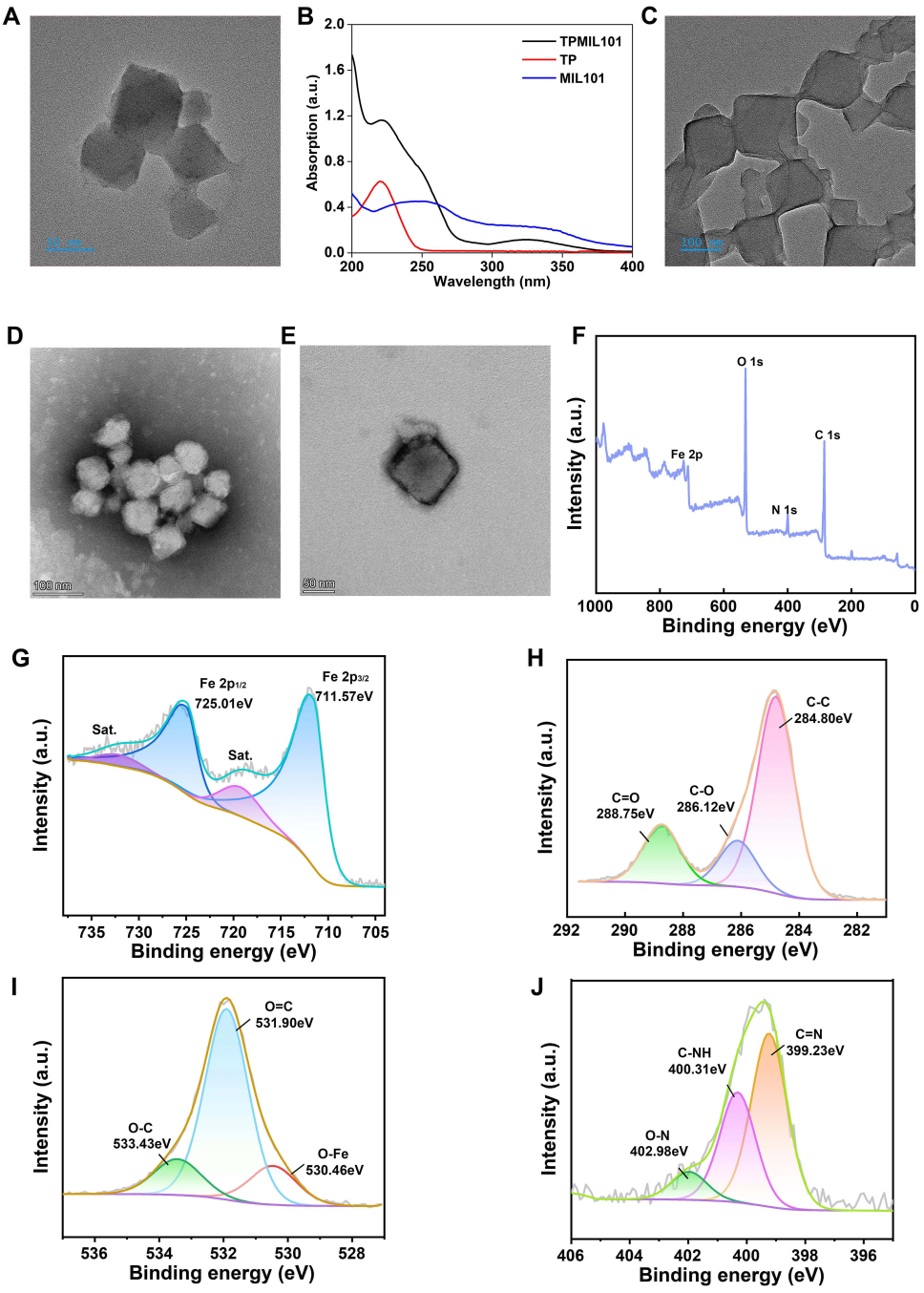

Figure 1 Characterization of TPMIL101-TCPP@Lip-HA. (**A**) TEM images of MIL101. (**B**) UV spectroscopic of TPMIL101. (**C**) TEM images of TPMIL101. (**D** and **E**) TEM images of TPMIL101-TCPP@Lip-HA. (**F**) Full XPS survey spectrum. Fe 2p: Signal peak generated by electron excitation from the iron 2p orbital, O 1s: Signal peak generated by electron excitation from the oxygen 1s orbital, N 1s: Signal peak generated by electron excitation from the nitrogen 1s orbital, C 1s: Signal peak generated by electron excitation from the carbon 1s orbital. (**G**) High-resolution Fe 2p spectrum. Fe $2p_1/_2$: Energy level corresponding to the total angular momentum quantum number j = 1/2 after spin–orbit coupling of the iron 2p orbital, Fe $2p_3/_2$: Energy level corresponding to the total angular momentum quantum number j = 3/2 after spin–orbit coupling of the iron 2p orbital. (**H**) High-resolution C 1s spectrum. C=O: Characteristic signal peak generated when a carbon atom is bonded to an oxygen atom via a double bond. C-O: Characteristic signal peak generated when a carbon atom is bonded to an oxygen atom via a single bond. C-C: Characteristic signal peak generated when a carbon atom is bonded to another carbon atom via a single bond. (**I**) High-resolution O 1s spectrum. O-C: Characteristic signal peak generated when an oxygen atom is bonded to a carbon atom via a single bond. O=C: Characteristic signal peak generated when an oxygen atom is bonded to a carbon atom via a double bond. O-Fe: Characteristic signal peak generated when an oxygen atom is coordinated to an iron atom. (**J**) High-resolution N 1s spectrum. O-N: Characteristic signal peak generated when a nitrogen atom is bonded to an oxygen atom. C-NH: Characteristic signal peak generated when a nitrogen atom is bonded to a carbon atom via a single bond and is also bonded to at least one hydrogen atom. C=N: Characteristic signal peak generated when a nitrogen atom is bonded to a carbon atom via a double bond.

https://doi.org/10.2147/IJN.S567165

Table 1 Hydrodynamic Size, PDI, and Zeta Potential of the Preparation

Type	Hydrodynamic Size (nm)	PDI	Zeta Potential (mV)
TPMIL101	173.83±12.77	0.17±0.01	16.43±0.48
TPMIL101@Lip	183.98±15.20	0.18±0.01	−12.54±1.03
TPMIL101-TCPP@Lip	189.10±9.19	0.17±0.01	−21.70±9.35
TPMIL101-TCPP@Lip-HA	190.40±9.35	0.16±0.01	−26.39±7.57

UV characteristic absorption peaks at 200 nm, 225 nm, and 330 nm (Figure 1B). The peaks at 200 nm and 330 nm correspond to MIL101, while the peak at 225 nm is attributed to TP, suggesting that TP has been effectively loaded into MIL101 nanoparticles without altering the structural characteristics of MIL101 (Figure 1C). The morphology of TPMIL101-TCPP@Lip-HA nanoparticles appeared as polyhedra, with liposome-coated nanoparticles observed (Figure 1D and E). Zeta potential results indicated that each material modification was accompanied by a potential change, particularly after liposome encapsulation, where the material's potential significantly reversed (Table 1). Dynamic light scattering (DLS) results demonstrated that the particle size of the nanomaterials gradually increased with group modification (Table 1), consistent with the TEM observations.

To determine the chemical composition of TPMIL101-TCPP@Lip-HA nanoparticles, X-ray photoelectron spectroscopy (XPS) was conducted. As illustrated in Figure 1F, the XPS full-scan map reveals peaks at 282.5, 397.0, 529.3, and 723.0 eV, corresponding to the photoelectron spectra of C1s, N1s, O1s, and Fe2p, respectively. This indicates that TPMIL101-TCPP@Lip-HA nanoparticles contain Fe, O, N, and C elements. In the fine photoelectron spectroscopy, $Fe2p_{3/2}$ and $Fe2p_{1/2}$ peaks of Fe elements were observed at 711.6 eV and 725.01 eV, respectively, accompanied by a satellite peak at approximately 719.8 eV (Figure 1G), which aligns with the characteristics of MIL101.[25] The C1s peaks can be attributed to C-C, C-O, and C=O bonds, with no other sub-peaks present (Figure 1H), confirming the presence of numerous TCPP molecules in the sample. A distinct O-Fe peak in the O1s sub-peaks confirms that TCPP molecules are connected via O-Fe bonds (Figure 1I). The N1s peaks were attributed to C=N, C-NH, and O-N (Figure 1J), verifying the presence of a substantial number of liposome molecules in the sample. These data further corroborate the successful synthesis of TPMIL101-TCPP@Lip-HA.

Release of TP and TCPP in vitro

The loading rate of TP in TPMIL101 was 8.76%. Following group modification and double loading, the loading ratio of TP in TPMIL101-TCPP@Lip-HA was 2.87%, while that of TCPP was 5.89%. TPMIL101-TCPP@Lip-HA was immersed in various PBS solutions to evaluate its decomposition release behavior. As illustrated in Figure 2A–C, the release of the drug TP and the photosensitizer TCPP was not influenced by acidity. Given that the MIL-101 material itself is formed by coordination, it exhibits instability in the PBS salt solution, and the observed drug release rate may be attributed to the degradation of MIL101 in the salt solution. After 24 h, TPMIL101 released approximately 83% of its TP (Figure 2A). Compared to the MIL101 preparation, the TP release rate of TPMIL101-TCPP@Lip-HA was relatively lower before 8 h (Figure 2B), potentially due to liposomes impeding the effect of PBS on MIL101. Generally, the TP release rate increased over time. This may be due to the exchange of salt ions inside and outside the phospholipid bilayer, leading to structural disruption of MIL101 and subsequent drug release. After 24 h, TPMIL101-TCPP@Lip-HA released about 82% and 68% of TP and TCPP, respectively (Figure 2B and C). The gradual release of TP and TCPP from TPMIL101-TCPP@Lip-HA nanoparticles is not affected by pH, which is conducive to their sustained anti-tumor activity.

•OH and ROS Generation Capacity of TPMIL101-TCPP@Lip-HA in vitro

The photocatalytic capacity of TPMIL101-TCPP@Lip-HA was evaluated before examining its ability to produce •OH or $^1O_2^-$ (Figure 2D). As a detector, TMB traps •OH in the solution, eventually forming a blue complex with an absorption peak at 652 nm.[26,27] As shown in Figure 2E, when H_2O_2 was added to the mixture of TPMIL101-TCPP@Lip-HA and TMB and placed for 5 min, no UV absorption peak was found. Under the same experimental conditions, after laser

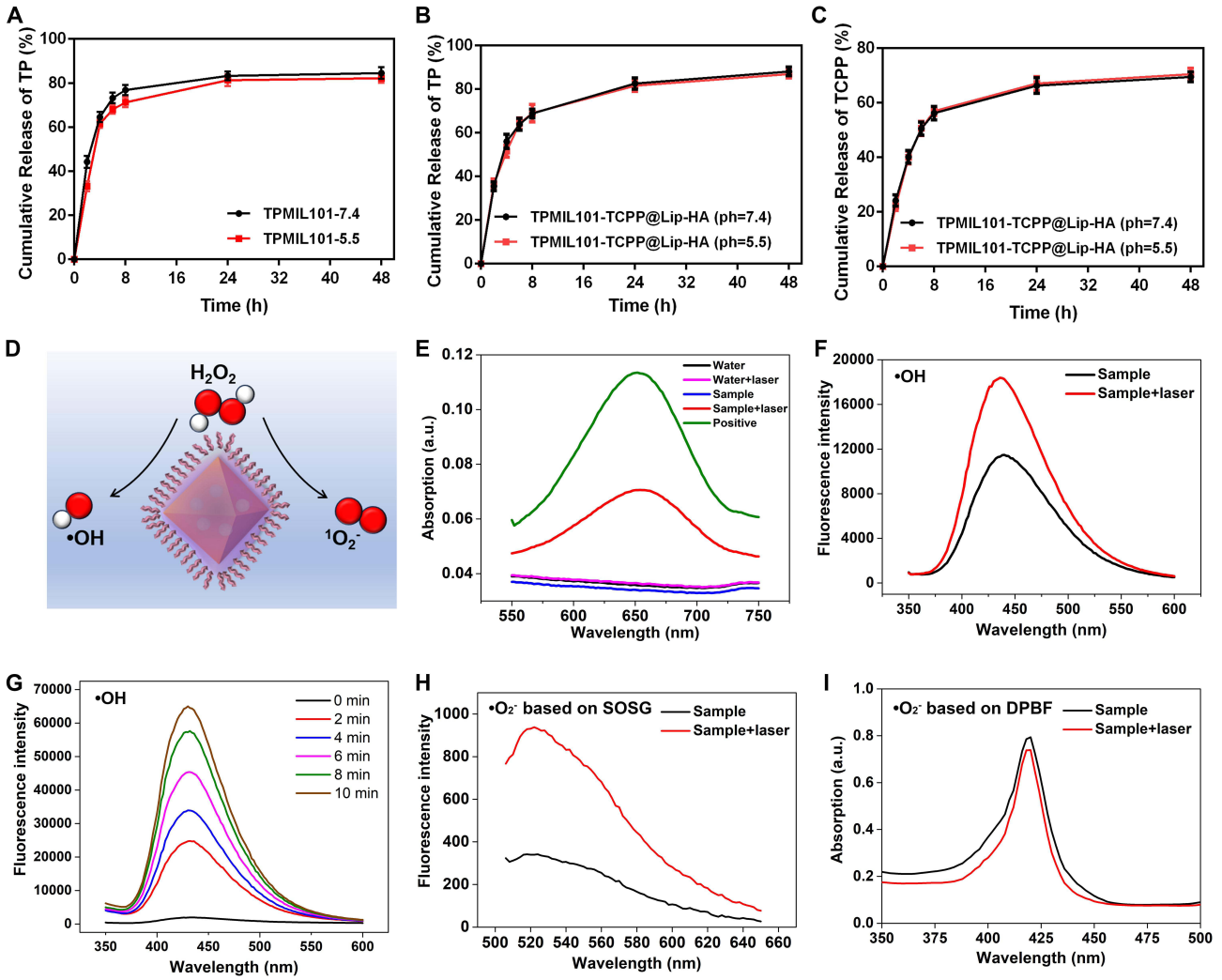

Figure 2 (**A**) TP release profiles in TPMIL101. (**B**) TP release profiles in TPMIL101-TCPP@Lip-HA. (**C**) TCPP release profiles in TPMIL101-TCPP@Lip-HA. (**D**) Schematic illustration of TPMIL101-TCPP@Lip-HA generates •OH and $^1O_2^-$. (**E**) UV–Vis absorb spectra about water or TPMIL101-TCPP@Lip-HA + H_2O_2 + TMB dispersed in water with or without laser radiation and peroxidase + H_2O_2 + TMB dispersed in water without laser radiation. (**F**) The level of •OH produced by TPMIL101-TCPP@Lip-HA with or without laser irradiation. (**G**) The level of •OH produced by TPMIL101-TCPP@Lip-HA at different time points with laser irradiation. (**H**) The level of $^1O_2^-$ produced by TPMIL101-TCPP@Lip-HA with or without laser irradiation was based on the SOSG probe. (**I**) The level of $^1O_2^-$ produced by TPMIL101-TCPP@Lip-HA with or without laser irradiation was based on the DPBF probe.

irradiation for 5 min, an obvious absorption peak was observed at 652 nm. TPMIL101-TCPP@Lip-HA plus laser irradiation shows the same effect as peroxidase, indicating that it has photocatalytic properties. In order to avoid the interference of the thermal effect produced by laser irradiation on positive results, deionized water was used as the control. No UV absorption peak was observed with or without laser irradiation.

To comprehensively assess the •OH generation capability of TPMIL101-TCPP@Lip-HA, H_2BDC was employed as a •OH collector to produce 2-hydroxyterephthalic acid.[24] As illustrated in Figure 2F, a strong fluorescence signal was observed in the TPMIL101-TCPP@Lip-HA group at 450 nm, which was significantly amplified following laser irradiation. This suggests that laser irradiation enhances TPMIL101-TCPP@Lip-HA's ability to generate substantial amounts of •OH. The fluorescence signal at 450 nm continued to increase with prolonged laser irradiation time. However, the rate of fluorescence intensity growth decelerated after 8 min of illumination (Figure 2G). These findings indicate that TPMIL101-TCPP@Lip-HA possesses inherent Fenton activity. It effectively catalyzes the decomposition of H_2O_2 into highly oxidative •OH under continuous 8-minute laser irradiation. Consequently, TPMIL101-TCPP@Lip-HA demonstrates significant potential for inducing tumor ferroptosis.

https://doi.org/10.2147/IJN.S567165

Subsequently, the ROS production capacity of TPMIL101-TCPP@Lip-HA was evaluated. SOSG probe, a green fluorescent probe highly selective to $^1O_2^-$ and unresponsive to other free radicals such as •OH and superoxide ion radical ($•O^{2-}$), was employed to detect $^1O_2^-$ production. As illustrated in Figure 2H, the characteristic peak intensity of the sample solution containing TPMIL101-TCPP@Lip-HA increased rapidly at 525 nm. Under laser irradiation, the intensity of the characteristic peak was further enhanced continuously. The ability of TPMIL101-TCPP@Lip-HA to produce $^1O_2^-$ was further assessed using a DPBF fluorescence probe. As anticipated, when the sample was co-incubated with the substrate, the absorbance of the sample after laser irradiation was significantly lower than that of the sample in the non-laser-treated group (Figure 2I). These findings suggest that TPMIL101-TCPP@Lip-HA in cooperate with laser irradiation could effectively catalyze the release of $^1O_2^-$, indicating a strong potential to induce tumor ferroptosis.

Evaluation of Antitumor Activity in vitro

HepG2 cells were employed to assess the antitumor efficacy of nanoparticles in vitro. CCK8 assay results demonstrated that cell proliferation in various drug groups was inhibited in a concentration-dependent manner (Figure 3A). Cell proliferation decreased most significantly following treatment with TPMIL101@Lip, TPMIL101-TCPP@Lip, and TPMIL101-TCPP@Lip-HA. At a drug concentration of 10 μg/mL, the cell viability rate approximated 50%. Compared to 10 μg/mL drug treatment alone, the cell viability rates in TPMIL101-TCPP@Lip and TPMIL101-TCPP @Lip-HA groups decreased significantly when drug treatment was combined with laser irradiation, while no significant difference was observed among TP, TPMIL101, and TPMIL101@Lip groups (Figure 3B). These findings suggest that without TCPP modification, laser irradiation did not significantly affect the cytotoxicity of nanoparticles. Calcein-AM/PI double staining was utilized to verify the cytotoxic activity of the nanoparticles, revealing that most cells in the TPMIL101-TCPP@Lip + L and TPMIL101-TCPP@Lip-HA + L groups were non-viable (Figure 3C and D). Notably, cell nuclear morphology in the TPMIL101-TCPP@Lip-HA + L group was severely altered, with some nuclei even disintegrating (Figure 3E). In conclusion, these results substantiate the potent cytotoxicity of the ferroptosis-synergized PDT therapeutic strategy.

The levels of ferroptosis induced by each nanoparticle were assessed. Compared to the control group or TP group, the intracellular Fe^{2+} concentration increased significantly after treatment with nanoparticles containing MOFs (TPMIL101, TPMIL101@Lip, TPMIL101-TCPP@Lip + L, TPMIL101-TCPP@Lip-HA + L; Figure 3F). High concentrations of Fe^{2+} and endogenous H_2O_2 can generate highly toxic hydroxyl radicals through the Fenton reaction in the TME.[28] Consequently, nanoparticles containing MOFs may induce ferroptosis in tumor cells. Compared to the control group or TP group, the green fluorescence intensity indicating ROS levels in TPMIL101-TCPP@Lip + L and TPMIL101-TCPP@Lip-HA + L groups was enhanced (Figure 3G and H), suggesting that the aberration of iron metabolism and the activation of photosensitizer may lead to ROS accumulation. The presence of numerous ROS can stimulate oxidative stress in tumor cells, induce lipid peroxidation, and ultimately lead to ferroptosis.[29] Therefore, the Fenton reaction in combination with PDT may cause higher levels of ferroptosis. GSH is a crucial antioxidant that maintains redox metabolic balance and protects cells from ROS-mediated damage.[30] GSH levels decreased in the TP group compared to the control group, suggesting that TP may inhibit GSH expression. Compared to the TP group, the intracellular GSH level in the TPMIL101-TCPP@Lip-HA + L group was significantly decreased (Figure 3I), possibly because a large amount of GSH in TEM was consumed while reducing Fe^{3+} to Fe^{2+}.[31] The decrease of GSH and the continuous increase of oxidative stress will cause the production of substantial LPO. As expected, various levels of LPO were observed to accumulate in the cells after nanoparticle treatment. The green fluorescence of the TPMIL101-TCPP@Lip-HA + L group was the strongest (Figure 3J and K), indicating that the production of LPO was the largest. MDA is one of the lipid peroxidation products during oxidative stress, and its accumulation is an important indicator of ferroptosis.[32,33] Compared to the other groups, the levels of MDA were significantly increased in the TPMIL101-TCPP@Lip-HA + L group (Figure 3L), suggesting that a higher level of ferroptosis occurred in this group. These results demonstrate that our designed drug delivery system can effectively induce ferroptosis in tumor cells by integrating the Fenton reaction and PDT strategy.

To investigate the effects of various nanoparticles on apoptosis, mitochondrial membrane potential was measured. As illustrated in Figure 4A and B, compared to the control group, mitochondrial membrane potential decreased after treatment with TP and nanoparticles, with TPMIL101-TCPP@Lip-HA + L treatment resulting in the most significant loss of 53.6%.

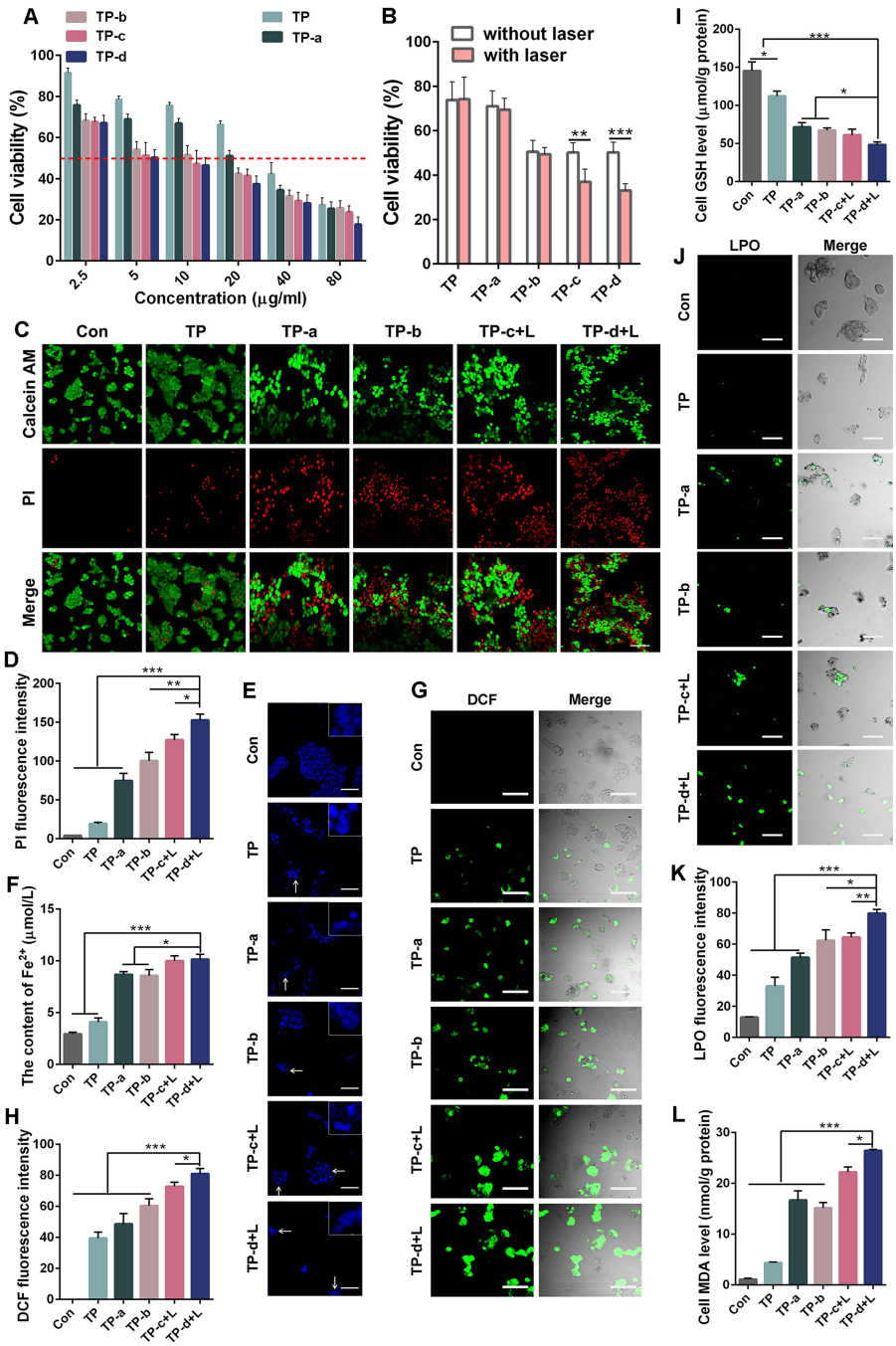

Figure 3 Evaluation of anti-HCC activity in vitro. (**A**) HepG2 cell viability after treatment with TP, TP-a, TP-b, TP-c, and TP-d at various concentrations for 24 h. Red dotted line: represents a cell survival rate of 50%. (**B**) HepG2 cell viability was treated with a drug concentration of 10 μg/mL under either laser irradiation or without laser irradiation. Significance was determined by unpaired Student's *t*-test and one-way analysis of variance, **P < 0.01, and ***P < 0.001. (**C**) Calcein-AM/PI staining was used to distinguish dead (red) and living (green) HepG2 cells after treatment with different formulations for 24 h. Scale: 100 μm. (**D**) Quantitative analysis of fluorescence intensities of PI after different treatments. Data are expressed as mean ± SD, n = 3 per group. Significance was determined by unpaired Student's *t*-test and one-way analysis of variance, *P < 0.05, **P < 0.01, and ***P < 0.001. (**E**) DAPI staining of HepG2 cell nuclei after being treated with different preparations for 24 h. White arrow: represents cells with abnormal nuclear morphology. Scale: 50 μm. (**F**) The levels of Fe^{2+} in HepG2 cells treated with different nano-preparations for 24 h. Data are expressed as mean ± SD, n = 6 per group. Significance was determined by unpaired Student's *t*-test and one-way analysis of variance, *P < 0.05, and ***P < 0.001. (**G**) Intracellular ROS staining of HepG2 cells after 24 h treatment with different formulations. Scale: 100 μm. (**H**) Quantitative analysis of fluorescence intensities of DCF after different treatments. Data are expressed as mean ± SD, n = 3 per group. Significance was determined by unpaired Student's *t*-test and one-way analysis of variance, *P < 0.05, and ***P < 0.001. (**I**) The levels of GSH in HepG2 cells treated with different nano-preparations for 24 h. Data are expressed as mean ± SD, n = 6 per group. Significance was determined by unpaired Student's *t*-test and one-way analysis of variance, *P < 0.05, and ***P < 0.001. (**J**) Intracellular LPO staining of HepG2 cells after 24 h treatment with different formulations. Scale: 50 μm. (**K**) Quantitative analysis of fluorescence intensities of LPO after different treatments. Data are expressed as mean ± SD, n = 3 per group. Significance was determined by unpaired Student's *t*-test and one-way analysis of variance, *P < 0.05, **P < 0.01, and ***P < 0.001. (**L**) The levels of MDA in HepG2 cells treated with different nano-preparations for 24 h. Data are expressed as mean ± SD, n = 6 per group. Significance was determined by unpaired Student's *t*-test and one-way analysis of variance, *P < 0.05, and ***P < 0.001. TP-a: represents TPMIL101, TP-b: represents TPMIL101@Lip, TP-c: represents TPMIL101-TCPP@Lip, TP-c + L represents TPMIL101-TCPP @Lip + laser, TP-d: represents TPMIL101-TCPP@Lip-HA, and TP-d + L represents TPMIL101-TCPP@Lip-HA + laser.

https://doi.org/10.2147/IJN.S567165

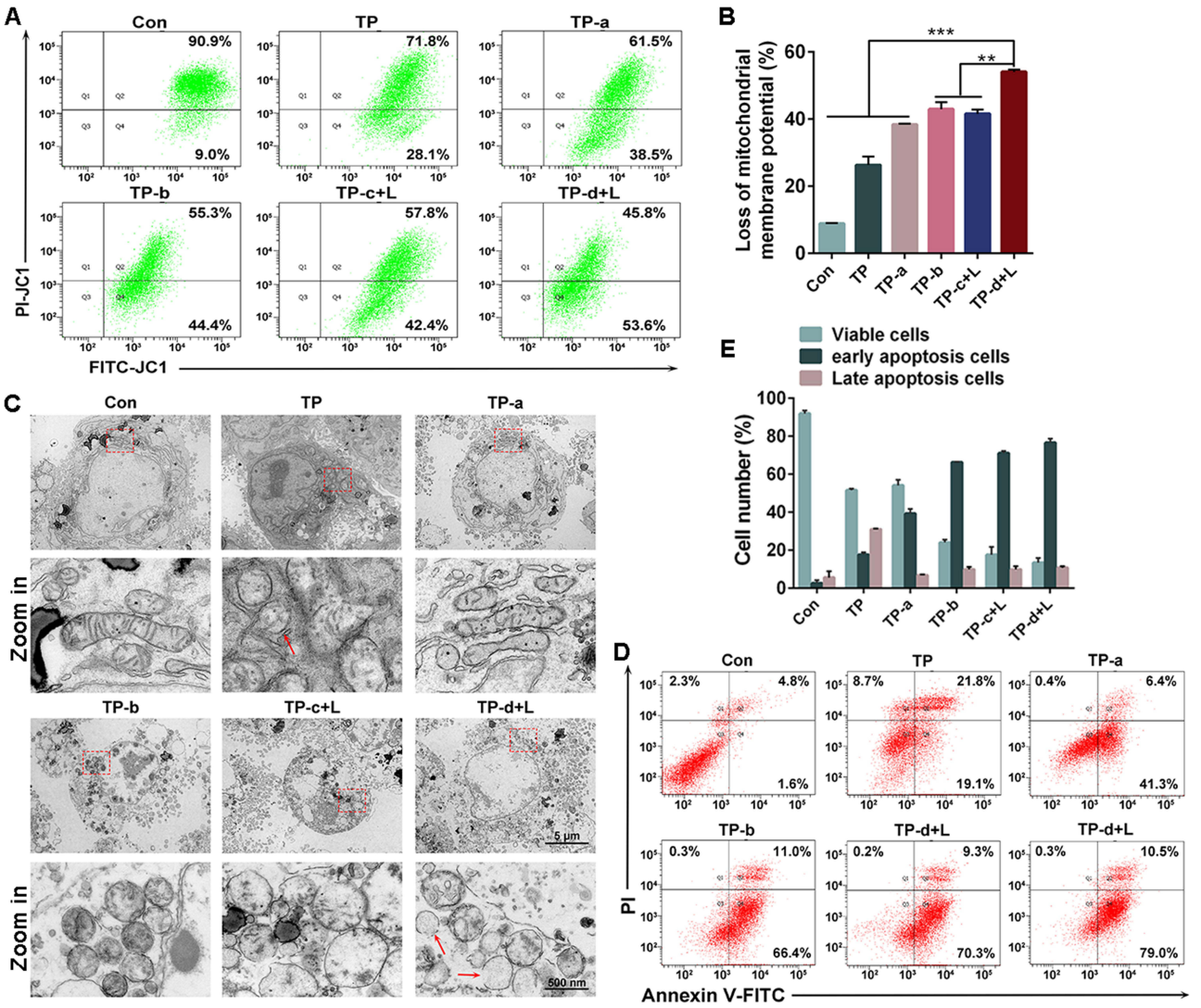

Figure 4 Evaluation of anti-HCC activity in vitro. (**A**) Measurement of the mitochondrial membrane potential of HepG2 cells treated with nano-preparations for 24 h, and (**B**) corresponding bar chart distribution and statistical analysis. Data are expressed as mean ± SD, n = 3 per group. Significance was determined by unpaired Student's *t*-test and one-way analysis of variance, **P < 0.01, and ***P < 0.001. (**C**) The mitochondrial morphological changes of HepG2 cells treated with nano-preparations for 24 h. Red dotted square boxes: represent the selected and zoom in regions, red arrows: indicate apoptotic characteristics in mitochondria, including swelling, blurred cristae, and membrane damage. (**D**) Annexin-V/PI apoptosis of HepG2 cells after 24 h treatment with nano-preparations, along with (**E**) the corresponding bar chart analysis of each group. TP-a: represents TPMIL101, TP-b: represents TPMIL101@Lip, TP-c: represents TPMIL101-TCPP@Lip, TP-c + L represents TPMIL101-TCPP@Lip + laser, TP-d: represents TPMIL101-TCPP@Lip-HA, and TP-d + L represents TPMIL101-TCPP@Lip-HA + laser.

Additionally, mitochondrial morphological changes in HepG2 cells treated with different nanoparticles were observed using biological TEM (Figure 4C). In contrast to the control group, the TP group exhibited apoptotic characteristics such as swelling, membrane damage, and indistinct mitochondrial cristae. The TPMIL101 and TPMIL101@Lip groups displayed clear ferroptosis features, including mitochondrial shrinkage and shallow or disappearing cristae, with these effects being more pronounced in the TPMIL101@Lip group. The TPMIL101-TCPP@Lip + L and TPMIL101-TCPP@Lip-HA + L groups demonstrated both ferroptosis and apoptotic typical features, such as mitochondrial swelling, membrane damage, and disappearing cristae, particularly evident in the TPMIL101-TCPP@Lip-HA + L group, corroborating the mitochondrial membrane potential results. Flow cytometry was employed to evaluate the impact of various nanoparticles on tumor cell apoptosis. Compared to the control group, the proportion of early apoptotic cells increased significantly in all nanoparticle groups, with TPMIL101-TCPP@Lip-HA + L treatment resulting in 79% early apoptotic cells (Figure 4D and E). TP treatment led to a more substantial change in the proportion of late apoptotic cells, suggesting that the constructed drug delivery platform can gradually release drugs to induce tumor cell apoptosis. In conclusion, these findings indicate that

https://doi.org/10.2147/IJN.S567165

TPMIL101-TCPP@Lip-HA + L can potently induce ferroptosis and apoptosis through the Fenton reaction in conjunction with PDT, thereby enhancing the toxic activity of TP on tumor cells.

Biological Distributional Behavior of TPMIL101-TCPP@Lip-HA in vivo

Before assessing the efficacy of TPMIL101-TCPP@Lip-HA against HCC in vivo, the biodistribution of the preparation was investigated using the HCC-CDX model. ICG and ICG/TPMIL101-TCPP@Lip-HA were administered via tail vein injection, and in vivo fluorescence was monitored. As illustrated in Figure 5A, the fluorescence intensity at the tumor site remained elevated for 48 hours post-injection, followed by a gradual decrease. The ICG/TPMIL101-TCPP@Lip-HA group exhibited higher fluorescence intensity at the tumor site compared to the ICG group at various time points, suggesting superior accumulation of nanoparticles at the tumor site relative to free drugs. After 120 h, the mice were euthanized, and fluorescence signals were detected in major organs and tumor tissues (Figure 5B). Fluorescence was primarily observed in tumor tissues, with minimal presence in the liver and kidney. This distribution may be attributed to nanoparticle uptake and renal metabolic pathways. Notably, the fluorescence intensity of tumor tissues in the ICG/TPMIL101-TCPP@Lip-HA group significantly exceeded that of the ICG group (Figure 5B). This finding further corroborates the efficient tumor accumulation of ICG/TPMIL101-TCPP@Lip-HA, which could enhance HCC treatment efficacy.

Evaluation of Antitumor Activity in vivo

Based on the in vitro therapeutic efficacy and biological distribution, the antitumor effect of TPMIL101-TCPP@Lip-HA in vivo was evaluated using the HCC-CDX model. The experimental procedure is illustrated in Figure 5C. Throughout the treatment period (days 1–13), tumor volume was recorded every 2 days to assess treatment efficacy. All administration groups effectively reduced tumor growth compared to the control group, with TPMIL101-TCPP@Lip-HA demonstrating the strongest inhibitory effect on tumors (Figure 5D). Notably, TPMIL101-TCPP@Lip-HA + L exhibited stronger antitumor activity than TPMIL101-TCPP@Lip-HA, a trend also observed between TPMIL101-TCPP@Lip and TPMIL101-TCPP @Lip + L groups. Tumors were photographed (Figure 5E), and tumor mass was recorded (Figure 5F). The TPMIL101-TCPP @Lip-HA + L group showed significantly smaller tumors compared to other groups. TP demonstrated a certain anti-tumor effect, with a tumor suppression rate (TSR) of 32.48%. The TSR values for TPMIL101, TPMIL101@Lip, TPMIL101-TCPP @Lip, TPMIL101-TCPP@Lip + L, TPMIL101-TCPP@Lip-HA, and TPMIL101-TCPP@Lip-HA + L were 51.07%, 68.76%, 76.30%, 90.63%, 89.62%, and 93.97%, respectively. All nanoparticle groups exhibited higher TSR than the TP group, indicating enhanced anti-tumor activity, consistent with in vitro treatment results. TCPP-modified nanoparticles combined with laser treatment (TPMIL101-TCPP@Lip + L and TPMIL101-TCPP@Lip-HA + L) demonstrated excellent anti-tumor efficacy, confirming the potent anti-tumor activity of ferroptosis combined with PDT treatment.

Throughout the treatment period, mice weights across all groups remained largely consistent, with no significant inter-group variations observed (Figure 5G). This stability suggests that the combination of nanomaterials and laser irradiation was well-tolerated. The impact of nanomaterials on hepatic and renal function was assessed through the measurement of serum biochemical markers (GPT, GOT, BUN, Cr). The synthesized nanomaterial did not induce acute liver or kidney damage. Moreover, compared to the free drug TP, it demonstrated reduced toxicity and enhanced safety (Figure 5H–K).

Following treatment, tumor samples from mice were collected and subjected to H&E, TUNEL, and Ki67 immunohistochemical staining. H&E results revealed significant alterations in the histopathological features of the tumors post-treatment, including varying degrees of nuclear aggregation and cytoplasmic extravasation. Notably, the TPMIL101-TCPP@Lip-HA + L group exhibited the most pronounced changes, characterized by loose cell arrangement, low cell density, and severe cellular damage (Figure 6A). TUNEL results corroborated these findings, demonstrating that TPMIL101-TCPP@Lip-HA + L treatment induced the most substantial apoptosis in tumor cells (Figure 6A and B). The extent of apoptosis positively correlated with the tumor inhibitory effect across all groups. Ki67, an established marker of cell proliferation activity,[34] showed an inverse correlation with the anti-tumor efficacy in tumor tissues. As anticipated, Ki67 expression decreased sequentially in the control group, TP, TPMIL101, TPMIL101@Lip, TPMIL101-TCPP@Lip, TPMIL101-TCPP@Lip-HA, TPMIL101-TCPP@Lip + L, and TPMIL101-TCPP@Lip-HA + L (Figure 6A and C).

Additionally, we examined the levels of proteins associated with ferroptosis (FTL, FTH, FSP1, GPX4, COX2) and apoptosis (BAX, BCL2, Cytochrome c, Cleaved Caspase 3) in the tumors. Following nanoparticle treatment, the

 https://doi.org/10.2147/IJN.S567165

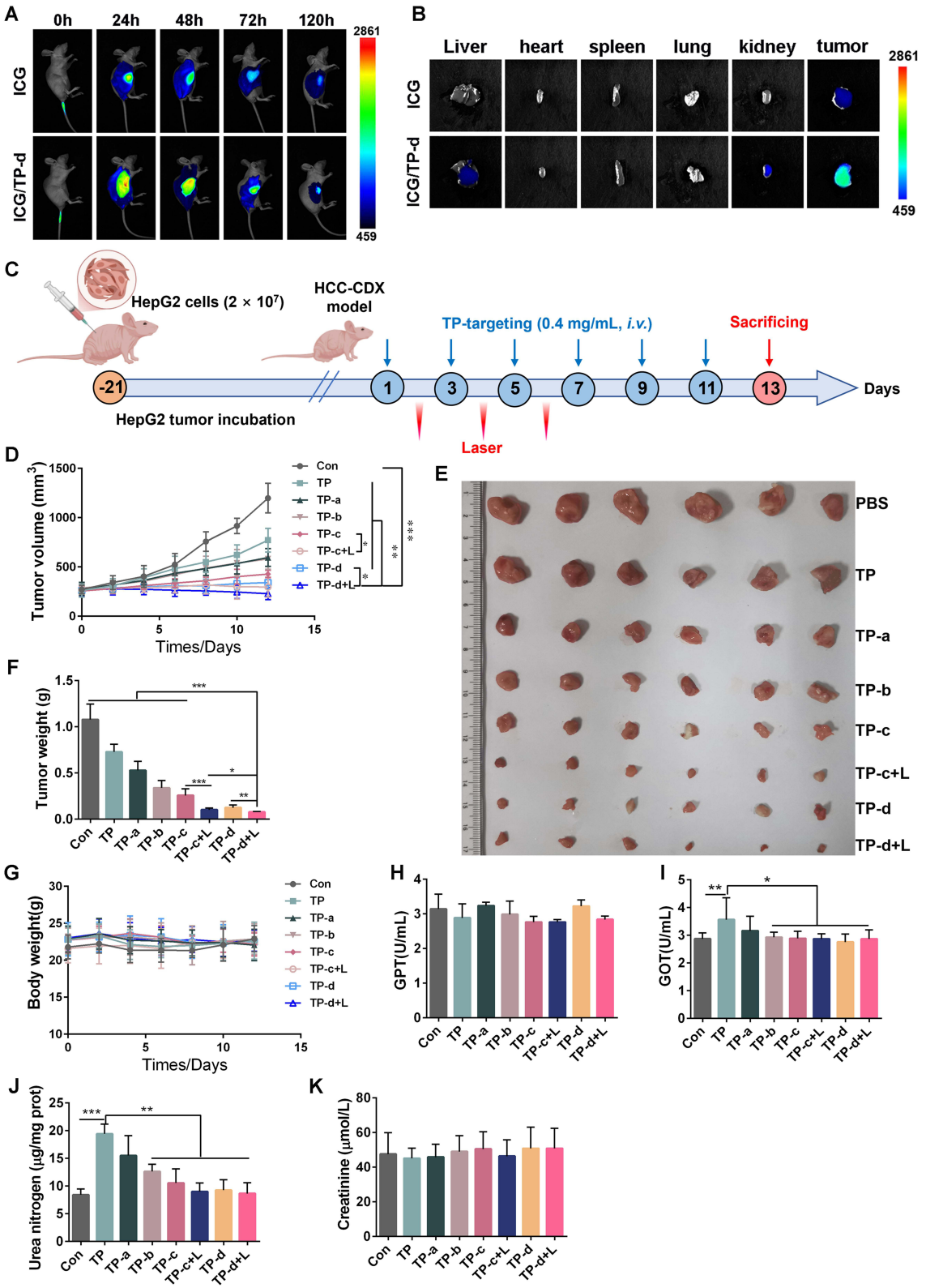

Figure 5 Evaluation of anti-HCC activity of different nano-preparations in vivo. (**A**) In vivo fluorescence images at different time points post-injection of ICG or ICG/TPMIL101-TCPP@Lip-HA. (**B**) Representative fluorescence images of excised major organs and tumors after tail vein injection of ICG or ICG/TPMIL101-TCPP@Lip-HA for 120 h. (**C**) Schematic illustration of the therapeutic scheme on the HCC-CDX model. (**D**) Tumor growth inhibition curves of mice after preparations were injected into the tail vein, n = 6 per group. (**E**) Photographs of the tumor. (**F**) The weight of tumors after treatment. (**G**) Changes in body weight during treatment. The levels of GPT (**H**), GOT (**I**), BUN (**J**), and Cr (**K**) in serum after treatment. Data are expressed as mean ± SD, n = 6 per group. Significance was determined by unpaired Student's *t*-test and one-way analysis of variance, *P < 0.05, **P < 0.01, and ***P < 0.001. TP-a: represents TPMIL101, TP-b: represents TPMIL101@Lip, TP-c: represents TPMIL101-TCPP@Lip, TP-c + L represents TPMIL101-TCPP@Lip + laser, TP-d: represents TPMIL101-TCPP@Lip-HA, and TP-d + L represents TPMIL101-TCPP@Lip-HA + laser.

https://doi.org/10.2147/IJN.S567165

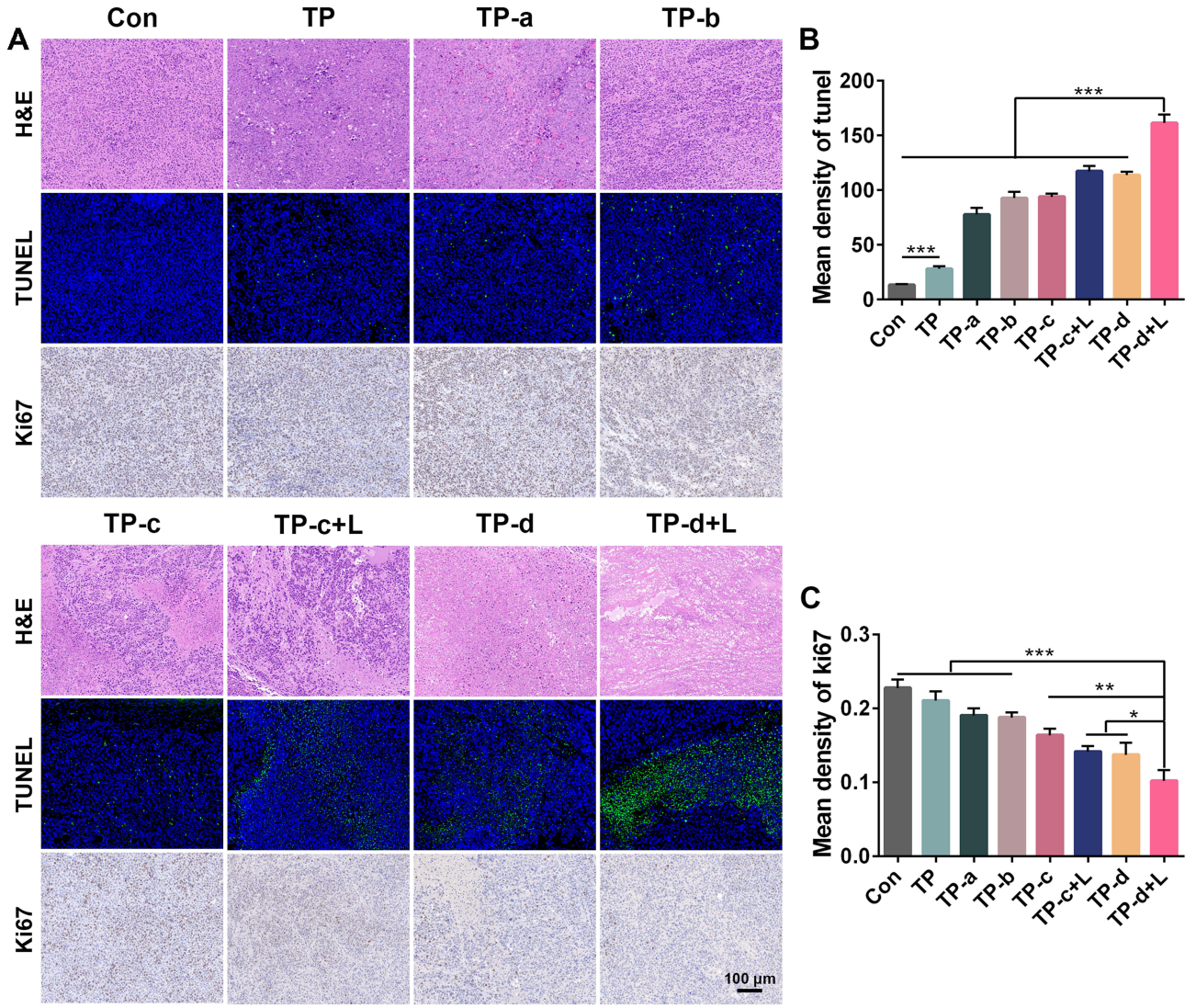

Figure 6 (**A**) H&E, TUNEL, Ki67 staining of the tumor after treatment. Quantitative analysis of TUNEL (**B**) and Ki67 (**C**). Data are expressed as mean ± SD, n = 3 per group. Significance was determined by unpaired Student's *t*-test and one-way analysis of variance, *P < 0.05, **P < 0.01, and ***P < 0.001. TP-a: represents TPMIL101, TP-b: represents TPMIL101@Lip, TP-c: represents TPMIL101-TCPP@Lip, TP-c + L represents TPMIL101-TCPP@Lip + laser, TP-d: represents TPMIL101-TCPP@Lip-HA, and TP-d + L represents TPMIL101-TCPP@Lip-HA + laser.

expression of FTL, FTH, and COX2 increased to varying degrees. The highest protein levels of FTL, FTH, and COX2 were observed in the TPMIL101-TCPP@Lip + L and TPMIL101-TCPP@Lip-HA + L groups (Figure 7A–D). Conversely, the expression levels of GPX4 and FSP1 decreased to different degrees, with the lowest levels observed in the TPMIL101-TCPP@Lip-HA + L group (Figure 7E–G). These findings suggest that TPMIL101-TCPP@Lip-HA may induce ferroptosis by upregulating the expression of intracellular iron-storage-related proteins and modulating the expression of oxidative stress proteins. After nanoparticle treatment, the expression levels of BAX, Cytochrome C, and Cleaved caspase 3 increased to varying degrees (Figure 7E, H–K). The relative levels in descending order are TPMIL101-TCPP@Lip-HA + L > TPMIL101-TCPP@Lip + L > TPMIL101@Lip or TPMIL101 > TP. A significant decrease in BCL2 protein level was observed in TPMIL101-TCPP@Lip-HA + L and TPMIL101-TCPP@Lip + L groups compared to the control group. These results indicate that TPMIL101-TCPP@Lip-HA may mediate tumor cell apoptosis through the cytochrome c/Apaf-1/caspase signaling pathway (The raw images of Western blot analysis in Figure 7 were shown in Supplementary Figures S2–S6).

https://doi.org/10.2147/IJN.S567165

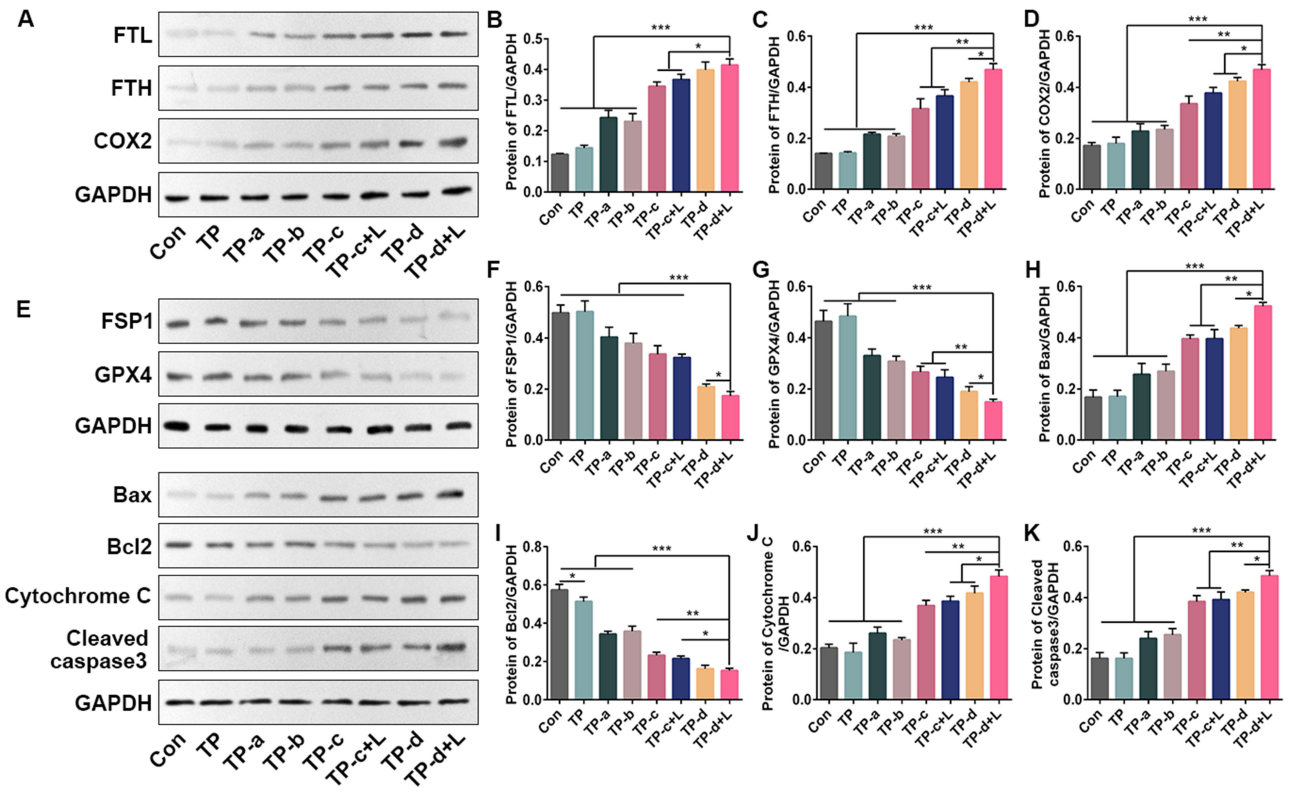

Figure 7 Molecular mechanism of ferroptosis synergism apoptosis in the treatment of HCC. Western blotting (**A** and **E**) and quantitative analysis (**B–D, F** and **G**) of ferroptosis-related proteins FTL, FTH, COX2, FSP1, and GPX4 in tumor tissue. Data are expressed as mean ± SD, n = 3 per group. Significance was determined by unpaired Student's *t*-test and one-way analysis of variance, *P < 0.05, **P < 0.01, and ***P < 0.001. Western blot (**E**) and quantitative analysis (**H–K**) of apoptosis-related proteins BAX, BCL2, Cytochrome C, and Cleaved caspase3 in tumor tissues. Data are expressed as mean ± SD, n = 3 per group. Significance was determined by unpaired Student's *t*-test and one-way analysis of variance, *P < 0.05, **P < 0.01, and ***P < 0.001. TP-a: represents TPMIL101, TP-b: represents TPMIL101@Lip, TP-c: represents TPMIL101-TCPP@Lip, TP-c + L represents TPMIL101-TCPP@Lip + laser, TP-d: represents TPMIL101-TCPP@Lip-HA, and TP-d + L represents TPMIL101-TCPP@Lip-HA + laser.

Discussion

HCC remains a therapeutic challenge due to its poor response to conventional treatments and unfavorable prognosis, necessitating the development of innovative therapeutic strategies. Emerging evidence highlights the potential of combining multiple cell death modalities as a promising approach to address tumor heterogeneity,[13,15,35,36] a strategy gaining traction in HCC clinical research. In this study, we propose a therapeutic approach leveraging the synergistic effects of ferroptosis and apoptosis, utilizing MIL101-TCPP@Lip-HA as a nanocarrier for the antitumor drug triptolide (TP). The TPMIL101-TCPP@Lip-HA platform demonstrates exceptional drug release kinetics, robust photosensitizer responsiveness, efficient tumor targeting, and excellent biocompatibility, as validated through drug release assays, in vitro ROS generation studies, and in vivo biodistribution analyses. This integrated strategy offers a promising avenue for enhancing HCC treatment efficacy.

Both in vitro and in vivo studies demonstrate that TPMIL101-TCPP@Lip-HA exhibits superior anti-HCC efficacy compared to free TP, attributed to its unique physicochemical properties. The nanoplatform enhances tumor accumulation through the EPR effect,[37] while its iron-based MOF framework continuously supplies Fe^{2+}, accelerating Fenton reactions. The tumor microenvironment (TME) further facilitates Fe^{3+} reduction to Fe^{2+} via GSH, establishing a Fe^{3+}/Fe^{2+} redox cycle[11] that generates cytotoxic •OH, driving ferroptosis.[28,38] Near-infrared laser irradiation activates the photosensitizer TCPP, producing abundant ROS to initiate photodynamic therapy (PDT). Elevated ROS levels oxidize unsaturated phospholipids, generating lipid peroxides (LPO) that synergistically enhance ferroptosis. Concurrently, mitochondrial damage and membrane potential loss trigger apoptosis. Importantly, TPMIL101-TCPP@Lip-HA encapsulation significantly reduces TP's systemic toxicity. Collectively, this nanoplatform achieves synergistic ferroptosis-apoptosis induction, effectively reducing tumor volume in HCC-CDX models and demonstrating remarkable potential for HCC therapy.

Western blot analysis of tumor tissues revealed the molecular mechanisms underlying TPMIL101-TCPP@Lip-HA's anti-HCC effects. Treatment with TPMIL101-TCPP@Lip-HA upregulated ferritin light chain (FTL) and ferritin heavy chain (FTH) while downregulating ferroptosis suppressor protein 1 (FSP1), suggesting enhanced intracellular Fe^{2+} accumulation via increased iron endocytosis and inhibited extracellular transport.[39,40] COX2 protein levels increased significantly, indicating severe oxidative stress in the tumor and substantial production of ROS and LPO, corroborating the in vitro confocal experiment result. GPX4, an intrinsic ferroptosis inhibitor, typically detoxifies lipid hydroperoxides to lipid alcohols.[41,42] This study observed decreased GPX4 protein levels, rendering it unable to neutralize toxic lipid peroxides produced by oxidative stress, leading to their accumulation. Consequently, excessive intracellular Fe^{2+} and LPO accumulation strongly induced ferroptosis in tumor cells. Multiple lines of evidence, including downregulation of GPX4, accumulation of LPO, elevation of intracellular Fe^{2+}, and characteristic mitochondrial alterations, collectively support the induction of ferroptosis. It should be noted, however, that in accordance with established mechanistic paradigms in ferroptosis research—such as rescue experiments employing specific inhibitors (eg., Ferrostatin-1)[43]—future studies are warranted to provide direct causal validation and unequivocally confirm the predominance of this cell death pathway. In parallel, TPMIL101-TCPP@Lip-HA treatment increased the intracellular BAX/BCL-2 ratio, resulting in the opening of mitochondrial permeability transport pores, increased membrane permeability, and cytochrome C release. This process triggered an intracellular Caspase cascade,[44] elevating caspase 3 expression. The subsequent destruction of cell-related structural and functional proteins led to DNA breakage and chromatin concentration, ultimately causing tumor cell apoptosis,[45] as observed in HE staining of tumor tissues. In conclusion, these results indicate that TPMIL101-TCPP@Lip-HA may induce tumor ferroptosis through intracellular Fe^{2+} and LPO overload, while simultaneously inducing mitochondrial apoptosis mediated by the cytochrome c/Apaf-1/caspase signaling pathway. The synergistic effect of ferroptosis and apoptosis demonstrated a potent anti-HCC efficacy.

In the present study, the hepatocellular carcinoma-derived xenograft (HCC-CDX) model using HepG2 cells provided a controlled and reproducible system for the initial in vivo validation of TPMIL101-TCPP@Lip-HA. However, its ability to fully recapitulate human HCC is inherently limited. This model lacks a functional immune system and fails to capture the complex tumor heterogeneity, stromal interactions, and pathophysiological features (eg., cirrhotic background) characteristic of clinical HCC.[46,47] These factors may influence drug delivery, therapeutic response, and the role of the tumor microenvironment in modulating ferroptosis and apoptosis. Despite these constraints, the findings from this model offer several clinically relevant insights. The study provides robust proof-of-concept that co-inducing ferroptosis and apoptosis via a rationally designed nanoplatform is a therapeutically viable strategy in vivo, achieving superior efficacy compared to the free drug. A key translational implication is the significant reduction in systemic toxicity afforded by the nanoformulation, as evidenced by preserved hepatic and renal function parameters. This directly addresses a major clinical limitation of TP—its narrow therapeutic index.[48] Furthermore, the demonstration of active tumor targeting (mediated by HA) and enhanced intratumoral accumulation lays a foundational principle for improving drug bioavailability and reducing off-target effects in solid tumors, a universal objective in oncological nanomedicine.[49] Thus, this work serves as a critical stepping stone. The compelling efficacy and safety profile observed in the HCC-CDX model justify and motivate future investigations in more clinically relevant models—such as patient-derived xenografts (PDXs) or immunocompetent murine models of HCC—to evaluate the platform's performance against tumor heterogeneity and its potential interactions with the immune system.

Beyond the current proof-of-concept, the TPMIL101-TCPP@Lip-HA platform opens several promising avenues for future research and clinical translation. The modularity of its design—composed of MOF, liposome, and hyaluronic acid—allows for the substitution of therapeutic agents (eg., other chemotherapeutics or immunomodulators) and targeting ligands, making it adaptable to other solid tumors with similar TME features. Given the emerging link between ferroptosis/apoptosis and antitumor immunity,[50,51] combining this platform with immune checkpoint inhibitors or other immunotherapies could further enhance therapeutic outcomes by stimulating systemic immune responses. The excellent biocompatibility and reduced systemic toxicity demonstrated here provide a strong foundation for future Good Manufacturing Practice (GMP)-compliant production, pharmacokinetic/toxicology profiling in higher-order animal models, and ultimately, clinical translation. Collectively, these directions highlight the versatility of TPMIL101-TCPP@Lip-HA as a multimodal nanotherapeutic platform with significant potential to address unmet clinical needs in HCC and beyond.

Conclusion

This study successfully developed and characterized a multifunctional nanodelivery platform, TPMIL101-TCPP@Lip-HA, designed for the co-delivery of TP and the photosensitizer TCPP to synergistically induce ferroptosis and apoptosis, thereby enhancing therapeutic efficacy against HCC. The platform demonstrated favorable stability, pH-independent drug release properties, significant tumor microenvironment responsiveness, and efficient tumor-targeting capability. In vitro experiments showed that TPMIL101-TCPP@Lip-HA efficiently generated ROS and •OH under near-infrared laser irradiation. Through the synergistic action of the Fenton reaction and PDT, it significantly increased intracellular levels of Fe^{2+}, LPO, and MDA, while reducing GSH content, effectively inducing ferroptosis in HepG2 cells. Decreased mitochondrial membrane potential, morphological alterations, and flow cytometry results further confirmed the concurrent activation of the apoptotic pathway. In an HCC-CDX mouse model, TPMIL101-TCPP@Lip-HA exhibited excellent tumor targeting and retention, achieving a tumor suppression rate of 93.97% when combined with laser irradiation, along with a significant reduction in the systemic toxicity of TP and no notable impact on hepatic or renal function. Histopathological and Western blot analyses revealed that the treatment upregulated iron storage proteins (FTL, FTH) and COX2 expression, downregulated GPX4 and FSP1, modulated the BAX/BCL-2 ratio, and activated the cytochrome c/Apaf-1/caspase signaling axis, thereby cooperatively triggering ferroptosis and mitochondrial apoptosis. In summary, TPMIL101-TCPP@Lip-HA integrates Fenton-driven ferroptosis and PDT-induced apoptosis, achieving synergistic activation of dual cell death pathways, which significantly enhances anti-HCC efficacy and improves safety.

Abbreviations

ANOVA, one-way analysis of variance; BUN, urea nitrogen; CDT, chemodynamic therapy; Cr, creatinine; DEE, drug encapsulation efficiency; DLC, drug loading capacity; DLS, Dynamic light scattering; DPBF, 1, 3-diphenyl isobenzofuran; GOT, glutamic-oxalic aminotransferase; GPT, glutamic-pyruvic aminotransferase; GSH, glutathione; H_2BDC, Terephthalic acid; $H_2BDC\text{-}NH_2$, 2-amino terephthalic acid; HCC, Hepatocellular carcinoma; HCC-CDX, hepatocellular carcinoma-derived xenograft; H&E, Hematoxylin and eosin; H_2O_2, hydrogen peroxide; ICG, Indocyanine green; LPO, lipid peroxides; MDA, Malondialdehyde; MOF, metal-organic framework; $^1O_2^-$, singlet oxygen; OD, optical density; $\bullet O^{2-}$, superoxide ion radical; •OH, hydroxyl radicals; PDI, polydispersity index; PDT, photodynamic therapy; ROS, reactive oxygen species; SD, standard deviation; SDT, sonodynamic therapy; SOSG, singlet oxygen sensor green; SPC, Soy phosphatidylcholine; TCPP, Mesotetra(4-carboxyphenyl)porphin; TMB, 3,3′,5,5′ -tetramethylbenzidine; TME, tumor microenvironment; TP, Triptolide; TSR, tumor suppression rate; TUNEL, transferase dUTP nick-end labeling; XPS, X-ray photoelectron spectroscopy; XRD, X-ray diffraction.

Data Sharing Statement

The data that supports the findings of this study are available from the corresponding author, Longfei Lin, upon reasonable request.

Ethics Statement

Male BALB/c nude mice (weighing 12-16 g) were used to evaluate the in vivo antitumor efficacy of the nanoformulation. The nude mice were purchased from Beijing SPF Biotechnology Co., Ltd. (license No. SCXK(Jing)2024-0001). The mice were housed in a specific pathogen-free animal laboratory under controlled conditions: constant temperature (~25 °C), constant humidity (~60%), and a 12-hour light/dark cycle. The ventilation rate was maintained at 15 air changes per hour, with an airflow speed ≤ 0.2 m/s at the cage level. Five mice were housed per cage on laminar-flow clean benches. Sterilized rodent feed and drinking water were provided, and cages and bedding were autoclaved before use. After a 3-day acclimatization period, the formal experiment commenced.

For the biodistribution study, mice were anesthetized via inhalation of 5% isoflurane (2 L/min flow rate) in an induction chamber before fluorescence imaging. Following the final fluorescence imaging session, mice were euthanized by cervical dislocation. In the antitumor efficacy assessment, anesthesia was similarly induced, followed by terminal blood collection via eyeball extraction, and euthanasia by cervical dislocation. All animal procedures strictly adhered to the *Regulations on the*

Management of Laboratory Animals and were approved by the Animal Ethics Committee of the Institute of Chinese Materia Medica, China Academy of Chinese Medical Sciences (Approval No. 2024B351). The authors adhered to the ARRIVE guidelines.

Funding

This work was supported by the Beijing Nova Program (20230484300), Fundamental Research Funds for the Central Public Welfare Research Institutes (ZZ13-YQ-059), and China Postdoctoral Science Foundation (2021M692732).

Disclosure

No potential conflict of interest was reported by the author(s).

References

1. Rumgay H, Arnold M, Ferlay J. et al. Global burden of primary liver cancer in 2020 and predictions to 2040. *J Hepatol*. 2022;77(66):1598–1606. doi:10.1016/j.jhep.2022.08.021
2. Liu Q. Triptolide and its expanding multiple pharmacological functions. *Int Immunopharmacol*. 2011;11:377–383. doi:10.1016/j.intimp.2011.01.012
3. Zhou ZL, Yang YX, Ding J, Li YC, Miao ZH. Triptolide: structural modifications, structure-activity relationships, bioactivities, clinical development and mechanisms. *Nat Product Report*. 2012;29:457–475. doi:10.1039/c2np00088a
4. Li R, Zhang Z, Wang J, et al. Triptolide suppresses growth and hormone secretion in murine pituitary corticotroph tumor cells via NF-kappaB signaling pathway. *Biomed Pharmacothe*. 2017;95:771–779. doi:10.1016/j.biopha.2017.08.127
5. Zhao X, Liu X, Zhang P, et al. Injectable peptide hydrogel as intraperitoneal triptolide depot for the treatment of orthotopic hepatocellular carcinoma. *Acta pharmaceutica Sinica B*. 2019;9:1050–1060. doi:10.1016/j.apsb.2019.06.001
6. Wu L, Pi W, Huang X, et al. Orchestrated metal-coordinated carrier-free celastrol hydrogel intensifies T cell activation and regulates response to immune checkpoint blockade for synergistic chemo-immunotherapy. *Biomaterials*. 2025;312:122723. doi:10.1016/j.biomaterials.2024.122723
7. Cao C, Wang X, Yang N, Song X, Dong X. Recent advances of cancer chemodynamic therapy based on Fenton/Fenton-like chemistry. *Chem Sci*. 2022;13:863–889. doi:10.1039/d1sc05482a
8. Lee SY, Park J, Jeong DI, et al. Ferrocene and glucose oxidase-installed multifunctional hydrogel reactors for local cancer therapy. *J Controll Rel*. 2022;349:617–633. doi:10.1016/j.jconrel.2022.07.017
9. Wang WJ, Ling YY, Zhong YM, Li ZY, Tan CP, Mao ZW. Ferroptosis-Enhanced Cancer Immunity by a Ferrocene-Appended Iridium(III) Diphosphine Complex. *Angew Chem Int Ed Engl*. 2022;61:e202115247. doi:10.1002/anie.202115247
10. Huo M, Wang L, Wang Y, Chen Y, Shi J. Nanocatalytic Tumor Therapy by Single-Atom Catalysts. *ACS nano*. 2019;13:2643–2653. doi:10.1021/acsnano.9b00457
11. He YJ, Liu XY, Xing L, Wan X, Chang X, Jiang HL. Fenton reaction-independent ferroptosis therapy via glutathione and iron redox couple sequentially triggered lipid peroxide generator. *Biomaterials*. 2020;241:119911. doi:10.1016/j.biomaterials.2020.119911
12. Zhang P, Qiao Y, Zhu L, et al. Nanoprobe Based on Biominerals in Protein Corona for Dual-Modality MR Imaging and Therapy of Tumors. *ACS nano*. 2023;17:184–196. doi:10.1021/acsnano.2c05917
13. Li Y, Qin Y, Shang Y, et al. Mechano-Responsive Leapfrog Micelles Enable Interactive Apoptotic and Ferroptotic Cancer Therapy. *Adv Funct Mater*. 2022;32:2112000. doi:10.1002/adfm.202112000
14. Zhang T, Sun Y, Cao J, et al. Intrinsic nucleus-targeted ultra-small metal-organic framework for the type I sonodynamic treatment of orthotopic pancreatic carcinoma. *J Nanobiotechnol*. 2021;19:315. doi:10.1186/s12951-021-01060-7
15. Chen Y, Chen Y, Wang Z, et al. Iron-based MOF with Catalase-like activity improves the synergistic therapeutic effect of PDT/ferroptosis/starvation therapy by reversing the tumor hypoxic microenvironment. *J Nanobiotechnol*. 2024;22:705. doi:10.1186/s12951-024-02921-7
16. Tu Z, Zhong Y, Hu H, et al. Design of therapeutic biomaterials to control inflammation. *Nature Rev Mater*. 2022;7:557–574. doi:10.1038/s41578-022-00426-z
17. Wang XQ, Wang W, Peng M, Zhang XZ. Free radicals for cancer theranostics. *Biomaterials*. 2021;266:120474. doi:10.1016/j.biomaterials.2020.120474
18. Li XY, Deng FA, Zheng RR, et al. Carrier Free Photodynamic Synergists for Oxidative Damage Amplified Tumor Therapy. *Small*. 2021;17:e2102470. doi:10.1002/smll.202102470
19. Tian J, Huang B, Nawaz MH, Zhang W. Recent advances of multi-dimensional porphyrin-based functional materials in photodynamic therapy. *Coord Chem Rev*. 2020;420:213410. doi:10.1016/j.ccr.2020.213410
20. Chen J, Zhu Y, Kaskel S. Porphyrin-Based Metal-Organic Frameworks for Biomedical Applications. *Angew Chem Int Ed Engl*. 2021;60:5010–5035. doi:10.1002/anie.201909880
21. Rabiee N, Yaraki MT, Garakani SM, et al. Recent advances in porphyrin-based nanocomposites for effective targeted imaging and therapy. *Biomaterials*. 2020;232:119707. doi:10.1016/j.biomaterials.2019.119707
22. Zhao J, Liu CS, Yuan Y, et al. Preparation of hemoglobin-loaded nano-sized particles with porous structure as oxygen carriers. *Biomaterials*. 2007;28:1414–1422. doi:10.1016/j.biomaterials.2006.10.012
23. Wang Z, Sun Q, Liu B, et al. Recent advances in porphyrin-based MOFs for cancer therapy and diagnosis therapy. *Coord Chem Rev*. 2021;439:213945. doi:10.1016/j.ccr.2021.213945
24. Ma X, Ren X, Guo X, et al. Multifunctional iron-based Metal-Organic framework as biodegradable nanozyme for microwave enhancing dynamic therapy. *Biomaterials*. 2019;214:119223. doi:10.1016/j.biomaterials.2019.119223
25. Yang B, Zhang Y, Sun L, et al. Modulated Ultrasmall γ-Fe2O3 Nanocrystal Assemblies for Switchable Magnetic Resonance Imaging and Photothermal-Ferroptotic-Chemical Synergistic Cancer Therapy. *Adv Funct Mater*. 2022;33. doi:10.1002/adfm.202211251

26. Fu C, Zhou H, Tan L, et al. Microwave-Activated Mn-Doped Zirconium Metal-Organic Framework Nanocubes for Highly Effective Combination of Microwave Dynamic and Thermal Therapies Against Cancer. *ACS nano*. 2018;12:2201–2210. doi:10.1021/acsnano.7b08868
27. Gao S, Lin H, Zhang H, Yao H, Chen Y, Shi J. Nanocatalytic Tumor Therapy by Biomimetic Dual Inorganic Nanozyme-Catalyzed Cascade Reaction. *Adv Sci*. 2019;6:1801733. doi:10.1002/advs.201801733
28. Zhang C, Bu W, Ni D, et al. Synthesis of Iron Nanometallic Glasses and Their Application in Cancer Therapy by a Localized Fenton Reaction. *Angew Chem Int Ed Engl*. 2016;55:2101–2106. doi:10.1002/anie.201510031
29. Chen J, Wang X, Zhang Y, et al. A redox-triggered C-centered free radicals nanogenerator for self-enhanced magnetic resonance imaging and chemodynamic therapy. *Biomaterials*. 2021;266:120457. doi:10.1016/j.biomaterials.2020.120457
30. Bao Z, Hua L, Ye Y, et al. MEF2C silencing downregulates NF2 and E-cadherin and enhances Erastin-induced ferroptosis in meningioma. *Neuro-Oncol*. 2021;23:2014–2027. doi:10.1093/neuonc/noab114
31. Hao YN, Qu CC, Shu Y, Wang JH, Chen W. Construction of Novel Nanocomposites (Cu-MOF/GOD@HA) for Chemodynamic Therapy. *Nanomaterials*. 2021;11:1843. doi:10.3390/nano11071843.
32. Louandre C, Ezzoukhry Z, Godin C, et al. Iron-dependent cell death of hepatocellular carcinoma cells exposed to sorafenib. *Int J Cancer*. 2013;133:1732–1742. doi:10.1002/ijc.28159
33. Yuan H, Li X, Zhang X, Kang R, Tang D. CISD1 inhibits ferroptosis by protection against mitochondrial lipid peroxidation. *Biochem Biophys Res Commun*. 2016;478:838–844. doi:10.1016/j.bbrc.2016.08.034
34. Wu J, Bremner DH, Niu S, et al. Chemodrug-Gated Biodegradable Hollow Mesoporous Organosilica Nanotheranostics for Multimodal Imaging-Guided Low-Temperature Photothermal Therapy/Chemotherapy of Cancer. *ACS Appl Mater Interfaces*. 2018;10:42115–42126. doi:10.1021/acsami.8b16448
35. Meng X, Li D, Chen L, et al. High-Performance Self-Cascade Pyrite Nanozymes for Apoptosis-Ferroptosis Synergistic Tumor Therapy. *ACS nano*. 2021;15:5735–5751. doi:10.1021/acsnano.1c01248
36. Zhang F, Li F, Lu G-H, et al. Engineering Magnetosomes for Ferroptosis/Immunomodulation Synergism in Cancer. *ACS nano*. 2019;13:5662–5673. doi:10.1021/acsnano.9b00892
37. Yu L, Wang Z, Mo Z, et al. Synergetic delivery of triptolide and Ce6 with light-activatable liposomes for efficient hepatocellular carcinoma therapy. *Acta pharmaceutica Sinica B*. 2021;11:2004–2015. doi:10.1016/j.apsb.2021.02.001
38. Liu G, Zhu J, Guo H, et al. Mo(2) C-Derived Polyoxometalate for NIR-II Photoacoustic Imaging-Guided Chemodynamic/Photothermal Synergistic Therapy. *Angew Chem Int Ed Engl*. 2019;58:18641–18646. doi:10.1002/anie.201910815
39. Trujillo-Alonso V, Pratt EC, Zong H, et al. FDA-approved ferumoxytol displays anti-leukaemia efficacy against cells with low ferroportin levels. *Nat Nanotechnol*. 2019;14:616–622. doi:10.1038/s41565-019-0406-1
40. Stockwell BR, Friedmann Angeli JP, Bayir H, et al. Ferroptosis: a Regulated Cell Death Nexus Linking Metabolism, Redox Biology, and Disease. *Cell*. 2017;171:273–285. doi:10.1016/j.cell.2017.09.021
41. Maiorino M, Conrad M, Ursini F. GPx4, Lipid Peroxidation, and Cell Death: discoveries, Rediscoveries, and Open Issues. *Antioxid Redox Signal*. 2018;29:61–74. doi:10.1089/ars.2017.7115
42. Yang WS, SriRamaratnam R, Welsch ME, et al. Regulation of ferroptotic cancer cell death by GPX4. *Cell*. 2014;156:317–331. doi:10.1016/j.cell.2013.12.010
43. Wu Y, Li C, Lu D, et al. Insulin-induced gene 2 alleviates ischemia-reperfusion injury in steatotic liver by inhibiting GPX4-dependent ferroptosis. *Cell Death Discovery*. 2025;11:127. doi:10.1038/s41420-025-02406-y
44. Wang H, Zhang C, Li M, et al. Antimicrobial Peptides Mediate Apoptosis by Changing Mitochondrial Membrane Permeability. *Int J Mol Sci*. 2022. doi:10.3390/ijms232112732
45. Zheng G-Y, Qu L-P, Yue X-Q, Gu W, Zhang H, Xin H-L. Portulacerebroside A induces apoptosis via activation of the mitochondrial death pathway in human liver cancer HCCLM3 cells. *Phytochem Lett*. 2014;7:77–84. doi:10.1016/j.phytol.2013.10.005
46. Li J, Wang X, Ren M, He S, Zhao Y. Advances in experimental animal models of hepatocellular carcinoma. *Cancer Med*. 2023;12:15261–15276. doi:10.1002/cam4.6163
47. Roth GS, Jílková ZM, Decaens T. Hepatocellular Carcinoma: animal Models Available to Characterize Tumor Immunology and Optimize Treatment Development. *J Cancer Immunol*. 2020;2(4):133–137.
48. Noel P, Von Hoff DD, Saluja AK, Velagapudi M, Borazanci E, Han H. Triptolide and Its Derivatives as Cancer Therapies. *Trends Pharmacol Sci*. 2019;40:327–341. doi:10.1016/j.tips.2019.03.002
49. Zhang R, Zhao X, Jia A, Wang C, Jiang H. Hyaluronic acid-based prodrug nanomedicines for enhanced tumor targeting and therapy: a review. *Int J Biol Macromol*. 2023;249:125993. doi:10.1016/j.ijbiomac.2023.125993
50. Zhou L, Lian G, Zhou T, et al. Palmitoylation of GPX4 via the targetable ZDHHC8 determines ferroptosis sensitivity and antitumor immunity. *Nat Cancer*. 2025;6:768–785. doi:10.1038/s43018-025-00937-y
51. Wiernicki B, Maschalidi S, Pinney J, et al. Cancer cells dying from ferroptosis impede dendritic cell-mediated anti-tumor immunity. *Nat Commun*. 2022;13:3676. doi:10.1038/s41467-022-31218-2